Diabatic Eddy Forcing Increases Persistence and Opposes Propagation of the Southern Annular Mode in MERRA-2

SAMUEL SMITH,[a,b] JIAN LU,[c] AND PAUL W. STATEN[b]

[a] *University of Chicago, Chicago, Illinois*
[b] *Indiana University Bloomington, Bloomington, Indiana*
[c] *Pacific Northwest National Laboratory, Richland, Washington*

(Manuscript received 14 February 2023, in final form 18 December 2023, accepted 17 January 2024)

ABSTRACT: As a dominant mode of jet variability on subseasonal time scales, the Southern Annular Mode (SAM) provides a window into how the atmosphere can produce internal oscillations on longer-than-synoptic time scales. While SAM's existence can be explained by dry, purely barotropic theories, the time scale for its persistence and propagation is set by a lagged interaction between barotropic and baroclinic mechanisms, making the exact physical mechanisms challenging to identify and to simulate, even in latest generation models. By partitioning the eddy momentum flux convergence in MERRA-2 using an eddy–mean flow interaction framework, we demonstrate that diabatic processes (condensation and radiative heating) are the main contributors to SAM's persistence in its stationary regime, as well as the key for preventing propagation in this regime. In SAM's propagating regime, baroclinic and diabatic feedbacks also dominate the eddy–jet feedback. However, propagation is initiated by barotropic shifts in upper-level wave breaking and then sustained by a baroclinic response, leading to a roughly 60-day oscillation period. This barotropic propagation mechanism has been identified in dry, idealized models, but here we show evidence of this mechanism for the first time in reanalysis. The diabatic feedbacks on SAM are consistent with modulation of the storm-track latitude by SAM, altering the emission temperature and cloud cover over individual waves. Therefore, future attempts to improve the SAM time scale in models should focus on the storm-track location, as well as the roles of the cloud and moisture parameterizations.

SIGNIFICANCE STATEMENT: As they circumnavigate the planet, the tropospheric jet streams slowly drift north and south over about 30 days, longer than the normal limit of weather prediction. Understanding the source of this "memory" could improve our knowledge of how the atmosphere organizes itself and our ability to make long-term forecasts. Current theories have identified several possible internal atmospheric interactions responsible for this memory. Yet most of the theories for understanding the jets' behavior assume that this behavior is only weakly influenced by atmospheric water vapor. We show that this assumption is not enough to understand jet persistence. Instead, clouds and precipitation are more important contributors in reanalysis data than internal "dry" mechanisms to this memory of the Southern Hemisphere jet.

KEYWORDS: Annular mode; Antarctic Oscillation; Dynamics; Diabatic heating; Jets; Subseasonal variability

1. Introduction

The most ubiquitous modes of variability in extratropical zonal winds are the barotropic "annular" modes, subseasonal-to-interannual fluctuations in tropospheric jet latitude that evoke a contracting and dilating annulus (Rossby and Willet 1948; Kidson 1988a; Thompson and Wallace 2000; Thompson et al. 2000). These annular dynamics are generated by a coherent shift of upper-tropospheric wave breaking and an associated shift of the eddy momentum flux convergence (EMFC), which drives the barotropic jets (Thompson and Wallace 2000; Lorenz and Hartmann 2001). Even highly idealized atmospheric models can reproduce the essential ingredients of annular modes (Lee and Feldstein 1996; Barnes et al. 2010; Lutsko and Hell 2021), evidence that they are both fundamental and theoretically established.

Given their low-frequency variability, barotropic annular modes (hereafter, annular modes) have been identified as a potential source of predictability in the atmosphere at longer-than-synoptic time scales (Kidson 1988b; Baldwin and Dunkerton 2001; Son and Lee 2006). Such efforts, however, have been complicated by difficulties in accurately simulating the annular mode time scale (Gerber et al. 2008), which is overpredicted even in latest generation models (Bracegirdle et al. 2020). Moreover, these model time scale biases have implications beyond predictability. Although there is much debate, these biases may imply an overestimation of the jet response to external forcing (Gritsun and Branstator 2007; Ring and Plumb 2008; Kidston and Gerber 2010; but also, Simpson and Polvani 2016; Hassanzadeh and Kuang 2016).

Perhaps the foremost mechanism to explain annular mode persistence is a positive eddy–jet feedback (Robinson 2000; Lorenz and Hartmann 2001; Simpson et al. 2013; Nie et al. 2014; Ma et al. 2017; Lubis and Hassanzadeh 2021). The

Supplemental information related to this paper is available at the Journals Online website: https://doi.org/10.1175/JAS-D-23-0019.s1.

Corresponding author: Samuel Smith, samuelsmith@uchicago.edu

DOI: 10.1175/JAS-D-23-0019.1

clearest evidence for the feedback is a positive correlation between the anomalous jet latitude and the annular mode–induced EMFC 7–10 days later (Lorenz and Hartmann 2001). However, the feedback does not appear in all seasons, and it is plausible that the proximate eddy–jet feedback is a manifestation of low-frequency variability, perhaps by way of the stratosphere (Byrne et al. 2016; Saggioro and Shepherd 2019). Nonetheless, eddy–jet feedbacks have been unambiguously demonstrated in idealized models forced with annular mode anomalies (Ma et al. 2017).

Another potential mechanism explains the increased persistence of annular modes as an interaction between the jet-shifting and jet-pulsing modes of variability (Lubis and Hassanzadeh 2021), typically defined as the first and second empirical orthogonal functions (EOFs) of zonal-mean zonal wind. While the two EOFs are uncorrelated at short lags (by construction), at longer lags, an equatorward shift of the jet is often preceded by a weakened jet and followed by a stronger jet. This interaction produces a slow meridional propagation of zonal wind anomalies (Lee et al. 2007; Sheshadri and Plumb 2017), and it explains the decreased annular mode time scale during propagation relative to the stationary regime (Lubis and Hassanzadeh 2021). Further, the decorrelation time scales of both EOFs can be predicted across all lags using only a single lag in the propagating system (Sheshadri and Plumb 2017), highlighting the coupled dynamics of the modes.

Given the endurance of time scale biases across model generations (Gerber et al. 2008; Simpson and Polvani 2016; Bracegirdle et al. 2020), improving the representation of annular mode time scales will require capturing higher-order dynamics than those represented in dry, idealized models. For example, recent work has suggested that the presence of moisture acts variously as a positive feedback on annular modes by selectively damping high-frequency eddies which shorten jet persistence (Lutsko and Hell 2021), or a negative feedback through the reduction of zonal-mean baroclinicity (Xia and Chang 2014).

Beyond the effects of condensational heating, cloud radiative effects (CRE) have also been suggested to affect the annular mode time scale because high clouds respond to shifts in the Southern Hemisphere jet (Thompson and Wallace 2000; Liu et al. 2020). Yet it remains unclear how CRE might feed back on the annular modes. Li et al. (2014) suggest CRE might decrease the annular mode time scale in the Northern Hemisphere, but Papavasileiou et al. (2020) find CRE weakly increase the time scale of its regional manifestation, the North Atlantic Oscillation. Notably, Papavasileiou et al. (2020) find significant positive feedbacks from latent heating and clear-sky heating on the North Atlantic Oscillation.

Since diabatic heating can influence EOF1 variability, it suggests diabatic heating may also influence the propagation of annular mode anomalies. In idealized models, radiative damping of large-scale eddies is partially responsible for the meridional propagation of zonal wind anomalies (Lee et al. 2007). In this model, propagation is primarily a barotropic process driven by slow shifts in the critical latitude for wave breaking. However, other idealized models suggest a balance between baroclinic processes and radiative damping drive propagation (Sparrow et al. 2009). The relative contributions of baroclinic, barotropic, and diabatic processes to the propagation of annular mode anomalies have yet to be determined.

The relative balance between processes for stationary modes of variability is also unclear. Upper-level barotropic shifts feedback onto the low-level baroclinicity, which increases in response to the enhanced surface friction and which helps maintain the upper-level anomaly (Robinson 2000; Blanco-Fuentes and Zurita-Gotor 2011; Zurita-Gotor et al. 2014). Diabatic heating damps this baroclinic response by modifying the low-frequency eddy forcing; suggesting an important but unclear role (Zurita-Gotor et al. 2014; Lutsko and Hell 2021). Nie et al. (2014; henceforth N14) attempt to resolve this using an eddy–mean flow interaction framework. However, their finding of primarily barotropic feedbacks neglects diabatic heating entirely, despite their framework's ability to quantify these impacts (Huang and Nakamura 2016).

The present work aims to address the following two questions. First, we seek to clarify the relative contributions of diabatic and other processes to the stationary regime in reanalysis data of the Southern Hemisphere, which has been the focus of many previous efforts to quantify eddy–jet feedbacks (Lorenz and Hartmann 2001; Simpson et al. 2013; N14) due to its relative zonal symmetry. Second, we examine the relative contributions of diabatic, baroclinic, and barotropic processes for the propagating regime of SAM variability. This further motivates examining SAM, as it exhibits both stationary and propagating regimes depending on the season (Sheshadri and Plumb 2017; and Fig. 2).

Using different seasons as proxies for stationary and propagating regimes of SAM, we apply an eddy–mean flow interaction framework extending and correcting the work of N14 to show that diabatic heating is the largest source of the eddy–jet feedback and the largest opposition to propagation in December–February (DJF). Additionally, baroclinic feedbacks, followed closely by diabatic feedbacks, are most important during March–November for the decorrelation time scale, while propagation is driven barotropically. Further, this work shows that the diabatic feedback in DJF is principally from clear-sky heating, while latent heating is more significant for the propagating regime in March–November. These diabatic feedbacks are likely a result of a shift in the latitude of wave generation with the jet, resulting in warmer and wetter eddies for equatorward jet shifts and colder and drier eddies for poleward jet shifts.

The rest of the work is outlined as follows. We begin by reviewing the finite-amplitude wave activity (FAWA) theory which allows us to quantify the contributions of diabatic heating to the combined pseudomomentum and mean flow (Nakamura and Zhu 2010), highlighting where our analysis improves upon N14. We then outline our methodology based on a partitioning of the EMFC. The results of this partitioning are presented first, followed by an analysis of where and how diabatic feedbacks are operating. We conclude with some reflections on utilizing our methodology as a part of a strategy to determine the source of model biases.

2. Theory

A simple budget for SAM results from the vertically integrated, zonal-mean zonal momentum balance in quasi-geostrophy (Lorenz and Hartmann 2001; N14):

$$\frac{d\langle\overline{u}\rangle}{dt} = M - \overline{X_s}, \tag{1}$$

where u is the zonal momentum, M is the EMFC, X_s is boundary layer friction, the overbar represent the zonal mean, and the angle brackets $\langle\cdot\rangle \equiv [1/(p_b - p_t)]\int_{p_b}^{p_t}(\cdot)\,dp$ represent vertical (mass-weighted) mean over the depth of the troposphere (1000–100 hPa). The EMFC is given by

$$M \equiv -\frac{1}{a\cos^2\phi}\frac{\partial}{\partial\phi}(\overline{u'v'}\cos^2\phi),$$

where the prime represents deviations from the zonal-mean, ϕ is latitude, a is the planetary radius, and v is meridional velocity. Notably, the EMFC in the extratropics is predominantly confined to be above 500 hPa and primarily geostrophic; thus, we can also write

$$\frac{d\langle\overline{u}\rangle}{dt} \approx \gamma\langle M\rangle_{500} - \overline{X_s} \equiv \gamma\langle M_g\rangle_{500} + \gamma\langle M_a\rangle_{500} - \overline{X_s}. \tag{2}$$

Now the integration of M is over 500–100 hPa, and we introduce a scale factor $\gamma \equiv 4/9$, given the relative mass of the upper troposphere to the entire troposphere (Lorenz 2023a). M_g is the geostrophic EMFC defined identically to M except utilizing the geostrophic wind:

$$M_g \equiv -\frac{1}{a\cos^2\phi}\frac{\partial}{\partial\phi}(\overline{u_g'v_g'}\cos^2\phi).$$

$M_a \equiv M - M_g$ is thus the ageostrophic component of M, and it is retained for reasons that will become evident. As in N14, we choose to focus on upper-level momentum because 1) the anomalous EMFC associated with SAM is concentrated above 500 hPa, 2) SAM is understood as primarily barotropic, and 3) this division enables us to understand contributions from the lower troposphere as they interface with the upper troposphere through the meridional heat flux.

To further probe SAM dynamics, we make use of the FAWA framework for eddy–mean flow interaction (Nakamura and Zhu 2010). FAWA applies a contour integral operator to quasigeostrophic (QG) potential vorticity (PV) q_g to quantify the pseudomomentum contained in large-scale eddies. FAWA (A) measures the amplitude of large-scale Rossby wave packets by integrating over the displacement of a PV anomaly from a conservative zonal symmetry (Q):

$$A \equiv A^S + A^N \equiv \left\{\frac{a}{2\pi\cos\phi_e}\iint\limits_{\substack{q>Q\\ \phi\le\phi_e}} q_g\cos\phi\,d\lambda\,d\phi\right\} + \left\{-\frac{a}{2\pi\cos\phi_e}\iint\limits_{\substack{q\le Q\\ \phi>\phi_e}} q_g\cos\phi\,d\lambda\,d\phi\right\}. \tag{3}$$

Here, ϕ_e is the equivalent latitude, the latitude an anomaly would have in conservative zonal symmetry. This zonal symmetry is found by dividing southward and northward PV displacements into regions of equal area, i.e., such that the area poleward of ϕ_e is equivalent to the area poleward of the PV contour it bisects. Thus, FAWA is an area-preserving integration. See Nakamura and Zhu (2010) or Huang and Nakamura (2016) for more detail.

In Eq. (3), A^S and A^N are wave activity from southward contour displacements and northward displacements, respectively. In the Southern Hemisphere, A^S is wave activity from large-scale anticyclonic waves ($q - Q > 0$), and A^N is from cyclonic waves ($q - Q < 0$). Because $A \ge 0$ by construction, we also define A^N as nonnegative, absorbing the difference in Eq. (3) into A^N, contrary to some definitions which define A^N as nonpositive.

Applying the integral operator in Eq. (3) to the PV budget results in a budget for wave activity [see Nakamura and Zhu (2010) and Nakamura and Solomon (2010) for derivations; compare to N14, Lu et al. (2015), Palipane et al. (2017)]:

$$\frac{\partial A}{\partial t} = -\overline{v_g'q_g'} - K^e_{\text{eff}}\frac{1}{a}\frac{\partial Q}{\partial\phi} + \Delta\Sigma. \tag{4}$$

The subscript g indicates the geostrophic component of the wind, $\Delta\Sigma$ represents diabatic and nonconservative sources of wave activity, and K^e_{eff} is the effective eddy diffusivity, representing the enhancement of the small-scale diffusive sink of wave activity by the large scale stretching of the material PV contour. K^e_{eff} must be diagnosed residually from Eq. (4).

Importantly, N14 assumes that $\Delta\Sigma$ is negligible to compute K^e_{eff}, given that diabatic heating is much smaller in the upper troposphere than the lower. However, we show that $\Delta\Sigma$ is not negligible, as coincidence between diabatic heating and upper-level waves enables diabatic injection of PV and subsequent modification of wave activity. This has significant consequences for the calculation of K^e_{eff} and the conclusions of N14, as we will show in section 4a.

The diabatic contributions to FAWA ($\Delta\Sigma$) are found by applying the integral operator in Eq. (3) to the PV source generated by differential vertical heating from diabatic sources (cf. Andrews et al. 1987; Palipane et al. 2017), or

$$\begin{aligned}\Delta\Sigma &\equiv \Delta\Sigma^S + \Delta\Sigma^N \\ &\equiv \left\{\frac{a}{2\pi\cos\phi_e}\iint\limits_{\substack{q>Q\\ \phi\le\phi_e}} f\frac{\partial}{\partial p}\left[\frac{(p_R p^{-1})^\kappa}{c_p d\tilde{\theta}/dp J_T}\right]\cos\phi\,d\lambda\,d\phi\right\} \\ &\quad + \left\{-\frac{a}{2\pi\cos\phi_e}\iint\limits_{\substack{q\le Q\\ \phi>\phi_e}} f\frac{\partial}{\partial p}\left[\frac{(p_R p^{-1})^\kappa}{c_p d\tilde{\theta}/dp}J_T\right]\cos\phi\,d\lambda\,d\phi\right\},\end{aligned} \tag{5}$$

where κ is the Poisson constant, c_p is the specific heat capacity at constant pressure, $p_R = 1000$ hPa is the reference pressure, $\tilde{\theta}(p)$ is the global-mean potential temperature, and J_T is the total diabatic heating rate, taken directly from output by the reanalysis (total temperature tendency due to physics/parameterizations). As with wave activity A, $\Delta\Sigma$ can be decomposed into cyclonic and anticyclonic contributions, keeping the same sign convention as discussed previously (i.e., $\Delta\Sigma^N$ is positive when acting as a source for A^N). $\Delta\Sigma$ can also be separately computed for the individual heating rates due to all-sky and

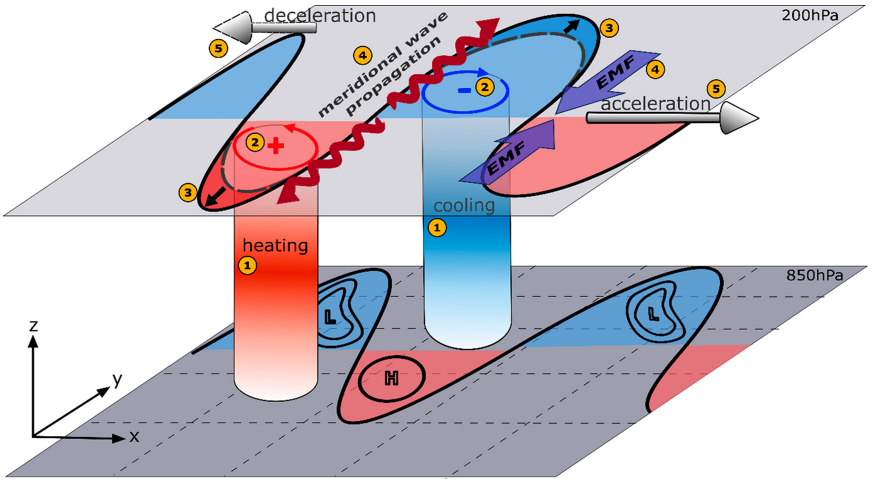

FIG. 1. Schematic depicting the diabatic injection of momentum in the Southern Hemisphere. See text for full description.

clear-sky radiative heating and condensation (each taken from the reanalysis, see section 3c).

Equation (5) can be scaled into a form identical to the vertical component of the Eliassen-Palm (EP) flux (see supplemental material), and thus, physically, diabatic heating generates momentum in a process akin to the baroclinic injection of momentum. We illustrate this schematically in Fig. 1. Diabatic heating, (1), generates PV through differential heating and the stretching of a column, (2). By injecting anomalous cyclonic PV into cyclonic waves, or anticyclonic PV into anticyclonic waves, or vice versa, diabatic heating generates or removes wave activity, (3). If the wave activity injection by diabatic heating propagates meridionally, then it induces an EMFC, (4), which accelerates or decelerates the zonal wind, (5).

Making use of the QG approximation that the meridional PV flux [first term on the rhs of Eq. (4)] balances the EP flux divergence, and also integrating vertically over the upper-troposphere (500–100 hPa), we can transform Eq. (4) to elucidate the connection between wave activity and zonal wind:

$$\frac{\partial\langle A\rangle_{500}}{\partial t} = -\langle M_g\rangle_{500} - f\left(\frac{\overline{v_g'\theta'}}{d\tilde{\theta}/dp}\right)\bigg|_{500} - \langle K^e_{\text{eff}}\rangle_{500}\frac{1}{a}\frac{\partial\langle Q\rangle_{500}}{\partial\phi} + \Delta\Sigma_{500}. \quad (6)$$

Here θ represents potential temperature, and f is the Coriolis parameter.

Multiplying Eq. (6) by the scale factor γ, we can combine it with Eq. (2) to produce a budget for the total momentum and wave activity:

$$\frac{d}{dt}(\langle\overline{u}\rangle + \gamma\langle A\rangle_{500}) = \gamma\langle M_a\rangle_{500} - \gamma f\left(\frac{\overline{v_g'\theta'}}{d\tilde{\theta}/dp}\right)\bigg|_{500} - \gamma\langle K^e_{\text{eff}}\rangle_{500}\frac{1}{a}\frac{\partial\langle Q\rangle_{500}}{\partial\phi} + \gamma\langle\Delta\Sigma\rangle_{500} - \overline{X_s}. \quad (7)$$

If one extends the integration in Eq. (7) over the entire troposphere, it becomes (ignoring M_a):

$$\frac{d}{dt}(\langle\overline{u}\rangle + \langle A\rangle) = \dot{A} - f\left(\frac{\overline{v_g'\theta'}}{d\tilde{\theta}/dp}\right)\bigg|_{1000} - \overline{X_s},$$

where $\dot{A}$ represents the combined effects of all nonconservative (diabatic and dissipative) sources/sinks of wave activity. Note that in the absence of nonconservative processes and in the barotropic limit (ignoring the boundary layer heat flux), the quantity $(\langle\overline{u}\rangle + \langle A\rangle)$ is conserved, making FAWA (A) a kind of pseudomomentum that has a tight inverse relationship with zonal momentum. [See Wang and Nakamura (2015) for the full baroclinic extension of this nonacceleration relation.] The negative covariation between FAWA and zonal wind is quite strong, even extending to a local conservation of pseudomomentum, particularly within storm track regions (Huang and Nakamura 2017; Nakamura and Huang 2018). Because of this tight connection, we will henceforth refer to pseudomomentum and FAWA interchangeably.

We can use Eq. (7) in the context of SAM to understand its evolution. Furthermore, when $\partial\langle A\rangle_{500}/\partial t = 0$, particularly during the eddy feedbacks which set SAM's time scale, we can partition the EMFC to understand the relative contributions of each process, akin to the partitioning first done by N14, but now more completely. Because of the strong inverse connection between FAWA and zonal momentum, N14 further argue that the negative wave activity tendency $(-\partial A/\partial t)$ can be construed as transient momentum fluctuations which do not feedback (or only weakly feedback) on the mean flow, akin to the stochastic portion of the EMFC $\tilde{m}$ of Lorenz and Hartmann (2001).

Thus, by comparing Eq. (7) with Eq. (1), we may partition the EMFC controlling SAM's dynamics as

$$\langle M\rangle_{500} = \underbrace{\frac{-\partial\langle A\rangle_{500}}{\partial t}}_{\text{transient}} - \underbrace{f\left(\frac{\overline{v_g'\theta'}}{d\tilde{\theta}/dp}\right)_{500}}_{\text{baroclinic}} - \underbrace{\left\langle K_{\text{eff}}^{e}\frac{1}{a}\frac{\partial Q}{\partial\phi}\right\rangle_{500}}_{\text{barotropic}} + \underbrace{\langle\Delta\Sigma\rangle_{500}}_{\text{diabatic}} + \langle M_a\rangle_{500}. \tag{8}$$

Equation (8) represents the decomposition for the EMFC into transient, barotropic, baroclinic, diabatic, and ageostrophic components. We drop the scale factor γ as all terms are integrated over the upper troposphere.

It should be noted here that Eq. (8) is a diagnostic equation, and that when the transient term $(-\partial\langle A\rangle_{500}/dt)$ is nonzero, we cannot determine the extent to which fluctuations in the EMFC are driving changes in FAWA or changes in FAWA are modulating the EMFC through the horizontal radiation of Rossby waves.[1] Further, as a diagnostic partitioning of the EMFC, one should not interpret the results of Eq. (8) as stating that removal of one of the processes on the rhs (such as in a dry or barotropic model) would remove an equal amount of momentum. Rather, Eq. (8) reveals the relative contributions of different processes in the highly coupled eddy–mean flow interaction problem containing exactly those processes. Understanding how Eq. (8) evolves during the life cycle of SAM reveals insights into the relative importance of said processes in determining its underlying dynamics. The climatological mean of Eq. (8) for MERRA-2 is shown in Fig. 1 in the online supplemental material.

The final step in utilizing Eq. (8) to analyze SAM is to project it onto SAM, following Simpson et al. (2013) and N14 (also see section 3a). Thus, we partition SAM's evolution and feedbacks by the various physical processes:

$$m_{\text{up}} = m_A + m_{\text{bt}} + m_{\text{bc}} + m_{\text{db}} + m_{\text{ag}}, \tag{9}$$

where m_A is the contribution from the (negative) wave activity tendency, m_{bt} he contribution from large-scale dissipation of FAWA through irreversible mixing (i.e., wave breaking), m_{bc} the baroclinic contribution from the meridional eddy heat flux from the lower troposphere, m_{db} the diabatic contribution, and m_{ag} the ageostrophic ones. Equation (9) is projected onto SAM because it allows us to utilize the framework of Lorenz and Hartmann (2001), found by projecting Eq. (2) onto the SAM:

$$\frac{dz}{dt} \approx \gamma m_{\text{up}} - \frac{z}{\tau}.$$

Here z is the SAM index, and the second term on the rhs results from parameterizing the frictional damping of SAM as Rayleigh damping at the boundary layer with time scale τ.

Finally, m_{db} can be further decomposed into various contributions as

$$m_{\text{db}} \equiv m_{\text{LH}} + m_{\text{LWCS}} + m_{\text{LWCRE}} + m_{\text{SWCRE}} + m_{\text{SWCS}}, \tag{10a}$$

$$\begin{aligned} m_{\text{db}} \equiv\ & m_{\text{LH}}^{S} + m_{\text{LH}}^{N} + m_{\text{LWCS}}^{S} \\ & + m_{\text{LWCS}}^{N} + m_{\text{LWCRE}}^{S} + m_{\text{LWCRE}}^{N} \\ & + m_{\text{SWCRE}}^{S} + m_{\text{SWCRE}}^{N} + m_{\text{SWCS}}^{S} + m_{\text{SWCS}}^{N}. \end{aligned} \tag{10b}$$

Here, subscripts on m denote the contribution from latent heating (LH), longwave clear-sky heating (LWCS), longwave cloud radiative heating (LWCRE), shortwave clear-sky heating (SWCS), and shortwave cloud radiative heating (SWCRE). Superscripts denote diabatic contributions in anticyclonic waves (S) and cyclonic waves (N).

3. Data and methods

a. SAM budget analysis

Following Simpson et al. (2013) and N14, we take the SAM indices as the first two EOFs of vertically integrated, zonal-mean zonal wind, including the area-based weighting of EOFs (Baldwin et al. 2009). We then project the wave activity budget onto each EOF spatial basis as $m = \mathbf{M}\cdot(\mathbf{W}\mathbf{e}_{1,2})\|\mathbf{W}^{1/2}\mathbf{e}_{1,2}\|^{-1}$, where $\mathbf{M}$ is a component of the budget, $\mathbf{W}$ is the weight matrix, and $\mathbf{e}_{1,2}$ are the EOF spatial patterns. We then perform lead-lag regressions of the projected terms onto the EOF time series ($z_{1,2}$). Decay time scales for each EOF are estimated by fitting an exponential curve to the autoregression of each time series. Lag-dependent time scales τ are estimated assuming an exponential decay of the autoregression ($C_{zz} \sim e^{-t/\tau}$) as $\tau \sim -1/(d\ln C_{zz}/dt)^{-1}$ after smoothing the derivative with a 7-point running mean (Zurita-Gotor et al. 2014). SAM feedbacks are calculated also following Simpson et al. (2013) and N14, as the ratio between the regression slope of each $m_{1,2}$ to the regression slope of $u_{1,2}$, which is the weighted projection of u onto each EOF.

PV is computed based on the full wind rather than only its geostrophic component, or $q_g \equiv (a\cos\phi)^{-1}[\partial_\lambda(v\cos\phi) - \partial_\phi(u\cos\phi)] + f\{1 + \partial_p[(\theta-\tilde{\theta})(d_p\tilde{\theta})^{-1}]\}$ (cf. Nakamura and Solomon 2010). This decision improves the numerical issues with computing the geostrophic wind (dividing by cos ϕ in subtropics/tropics, strong height gradients near the surface/topography) and results in a cleaner computation of wave activity based on q_g as described below. This choice reduces error in the computation of FAWA at the expense of increased error in the closure of the budget, but it does not strongly impact our results (see section 4a).

Wave activity integrations described above are carried out through a careful, geo-located sorting of the PV field to find the zonally symmetric reference PV, followed by a gridcell-counting procedure to determine the displacement. Diabatic PV source fields are integrated over the same area, following Smith et al. (2021). PV source fields are computed using the integrand in Eq. (5) from diabatic heating rates taken directly from the reanalysis output (see section 3c).

[1] It is worth noting, however, that Huang and Nakamura (2017) find a stronger covariation between FAWA and zonal momentum than between either FAWA and EMFC or zonal wind and EMFC, suggesting that the EMFC is not a principal driver of FAWA.

A composite of propagating events is made following a modification of the procedure outlined in Lee et al. (2007; see their section 4). We identify middle times of candidate events as any time where zonal wind anomalies are a local maximum at 50°S. Local maxima are identified as the maxima during a period beginning when the wind anomalies at 50°S are greater than 1 standard deviation above the mean and ending when anomalies have dipped below that value for at least 3 days. To remove propagation events that have anomalously short periods, the only local maxima retained must be a local maximum over a 70-day period centered on the candidate maximum. The remaining local maxima are taken to be the middle times of propagating events, of which we identify 81.

The 90% confidence intervals for each budget term are produced via bootstrapping. We generate 1000 random subsets of budget time series data (consecutively, with replacement) of length 2555 days (~7 years). All regressions are performed with each subset, selecting the 5th and 95th percentiles of the subsets as confidence interval bounds.

b. Analysis of breaking waves

We further investigate the physical mechanisms behind diabatic influences on SAM through an analysis of nonlinear, breaking waves. Waves are identified here as regions above the 90th percentile for a given month in both cyclonic and anticyclonic wave activity separately, located between 25° and 75°S. Identified regions must also be at least 500 000 km^2 in size to remove small-scale contributions to wave activity.

After computing the center of mass of a large wave activity region, we interpolate all fields to a 3000 km × 3000 km locally Cartesian grid centered at the wave activity centroid (given in *equivalent* latitude) to capture the entire wave region. Fields are averaged over the domain and vertically from 500 to 100 hPa for all identified wave events, and then regressed against the year-round SAM (EOF1) index.

c. Data source

Data for this work are obtained from NASA MERRA-2. MERRA-2 data are gridded at approximately 0.5° latitude × 0.625° longitude resolution, with 29 vertical levels between surface and midstratosphere (30 hPa). Further details can be found in Gelaro et al. (2017). MERRA-2 was chosen for this work because it provides different diabatic heating rates and fast accessibility. Due to storage constraints, a recent 15 years of 6-hourly data, 2005–19, were selected. These high-frequency data are needed to resolve medium-scale waves (periods around 2 days) which contribute to SAM (Ma et al. 2017). Because we can identically reproduce N14's results, which utilized a different and longer dataset (see supplemental Fig. 2), we do not expect that our choice of dataset or temporal range are strongly impacting our results.

Data downloaded are horizontal velocity, geopotential height, temperature, surface pressure, and temperature tendencies due to longwave, longwave clear-sky, shortwave, shortwave clear-sky, moist processes, and physics. Cloud heating rates are diagnosed simply as all-sky rates minus clear-sky rates.

4. Results and discussion

a. SAM pseudomomentum budgets

We begin our discussion by recognizing that SAM exhibits different behavior in different seasons (Sheshadri and Plumb 2017; also Fig. 2). MAMJJASON shows all the hallmarks of propagation: 1) cross-correlations between EOF1 and EOF2, 2) a similar decay time scale between EOFs 1 and 2, and 3) a similar fraction of variance explained by both EOFs (Lee et al. 2007; Sheshadri and Plumb 2017; Lubis and Hassanzadeh 2021). In contrast, DJF shows: 1) weak cross-EOF correlations, 2) an EOF1 time scale almost double that of EOF2, and most importantly, 3) more than twice the variance explained by EOF1 than by EOF2. [The threshold ratio for discriminating between regimes is 2:1; see Lee et al. (2007).] Physically, the stationary regime is associated with single jet climates when the eddy-driven jet is weak, such as during summer, and the propagating regime tends to form when the eddy-driven jet is stronger and displaced from the subtropical jet, as in most of the rest of the year (Lee et al. 2007). We proceed using DJF as a proxy for the stationary regime, and MAMJJASON as a proxy for the propagating regime. (Data are detrended and de-seasonalized before examining their relationship with SAM.)

Based on the implied decorrelation time scale (solid lines in Figs. 2c,d), we focus on processes at lag day 10 throughout this analysis. This results from a compromise between the different peaks in feedbacks for EOFs 1 (day 9) and 2 (day 12) and the need to avoid the stochastic forcing of synoptic eddies at short time scales and the weak correlations at long lags. We also aim to capture the interactions between EOFs, which peak around day 10 for MAMJJASON. While choosing to focus on a single lag day of 10 results in EOF2 feedbacks that are somewhat weak, it greatly simplifies the analysis by enabling consideration of feedbacks and propagation simultaneously.

Prior to lag day 0 during the generation of EOFs 1 and 2, SAM is primarily barotropic and transient in both seasons (Figs. 3a,b), consistent with N14 and expectation (Thompson and Wallace 2000). The barotropic nature of the propagating regime stands out, where almost the entire peak (lag day −1) comes from m_A and m_{bt} for both EOFs. The positive m_A reflects a decrease in wave activity poleward of the jet and increase in wave activity equatorward of it during poleward SAM, and oppositely for equatorward SAM. This is consistent with the inverse relationship between FAWA and zonal wind (Wang and Nakamura 2015; Nakamura and Huang 2018). However, as discussed in section 2, where m_A is large, m_{up} may be driving m_A rather than the other way around, suggesting caution when interpreting the budget during SAM's generation. Despite this, given good agreement with previous work and with theory (N14; Thompson and Wallace 2000), interpreting the EMFC as predominantly barotropic and transient seems reasonable. Given the strong negative correlation between wave activity and zonal velocity, we also interpret the pulsing variability (EOF2) in Figs. 3e and 3f as primarily transient during its generation (short negative lags).

This transience continues for short positive lags (lag days 0–3) and may be connected to the transient negative feedbacks described by Lorenz (2023b), where the rapid adjustments of the

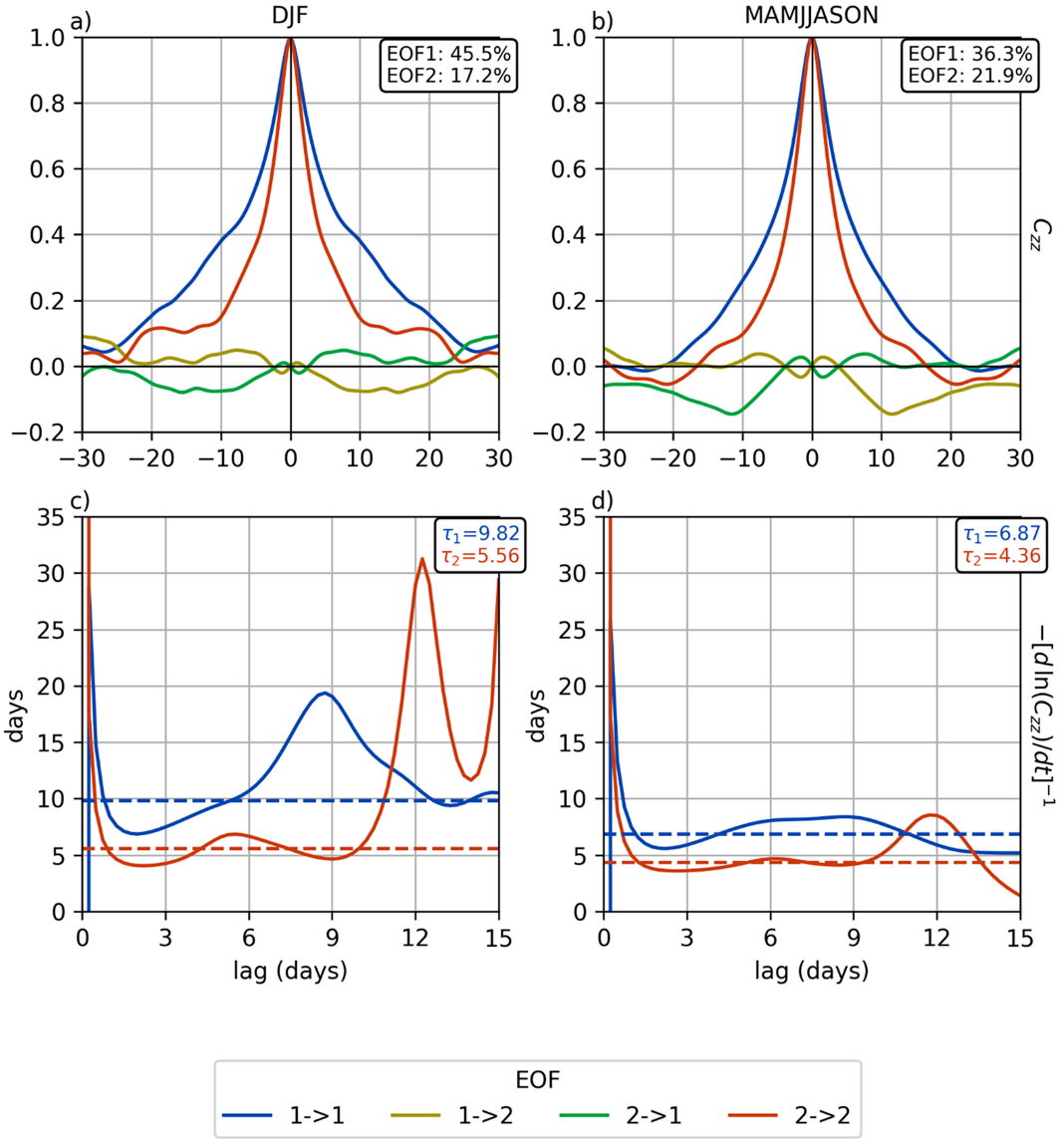

FIG. 2. (top) Lead–lag regressions of EOF 1 and 2 time series of zonal wind onto themselves and each other for (a) December–February (DJF) and (b) March–November (MAMJJASON) from 2005 to 2019 in MERRA-2. Also listed is the variance explained by each mode (normalized eigenvalue). (bottom) The smoothed, implied decorrelation time scale (assuming exponential decay) for the EOF 1 and 2 autocorrelations as a function of lag (solid lines) for (c) DJF and (d) MAMJJASON, as well as the mean decorrelation time scale produced by fitting an exponential decay function to the autocorrelations in (a) and (b).

eddy field to the new mean flow result in a damping of zonal wind variability. Because the change in the FAWA tendency primarily captures the rapid response of synoptic and planetary waves to the new mean flow, we believe this is consistent with Lorenz (2023b) and with Robert et al. (2017) who note the importance of both types of waves for the negative feedback. Lorenz (2023b) also demonstrates that this negative feedback is stronger for EOF2, in part explaining its lack of a long-term positive feedback. Here, we also find that the negative feedbacks (barotropic and transient feedbacks) are stronger at shorter lags (6–8 days) for EOF2 (Figs. 3g,h) than for EOF1 (Figs. 3c,d). This is further evidence that our decomposition can be connected to and can quantify SAM's relevant mechanisms identified by previous literature.

Interestingly, diabatic heating is adding pseudomomentum in phase with SAM during its generation, particularly during DJF. This could be evidence of a diabatic reinforcement of SAM by damping wave activity equatorward of the jet and generating it poleward of the jet during equatorward SAM, assuming a complete conversion of the source and the inverse relationship between FAWA and zonal wind, which would "boost" the barotropic dynamics responsible for SAM. Alternatively, if diabatic heating is generating wave activity equatorward of the jet and the wave activity is propagating meridionally

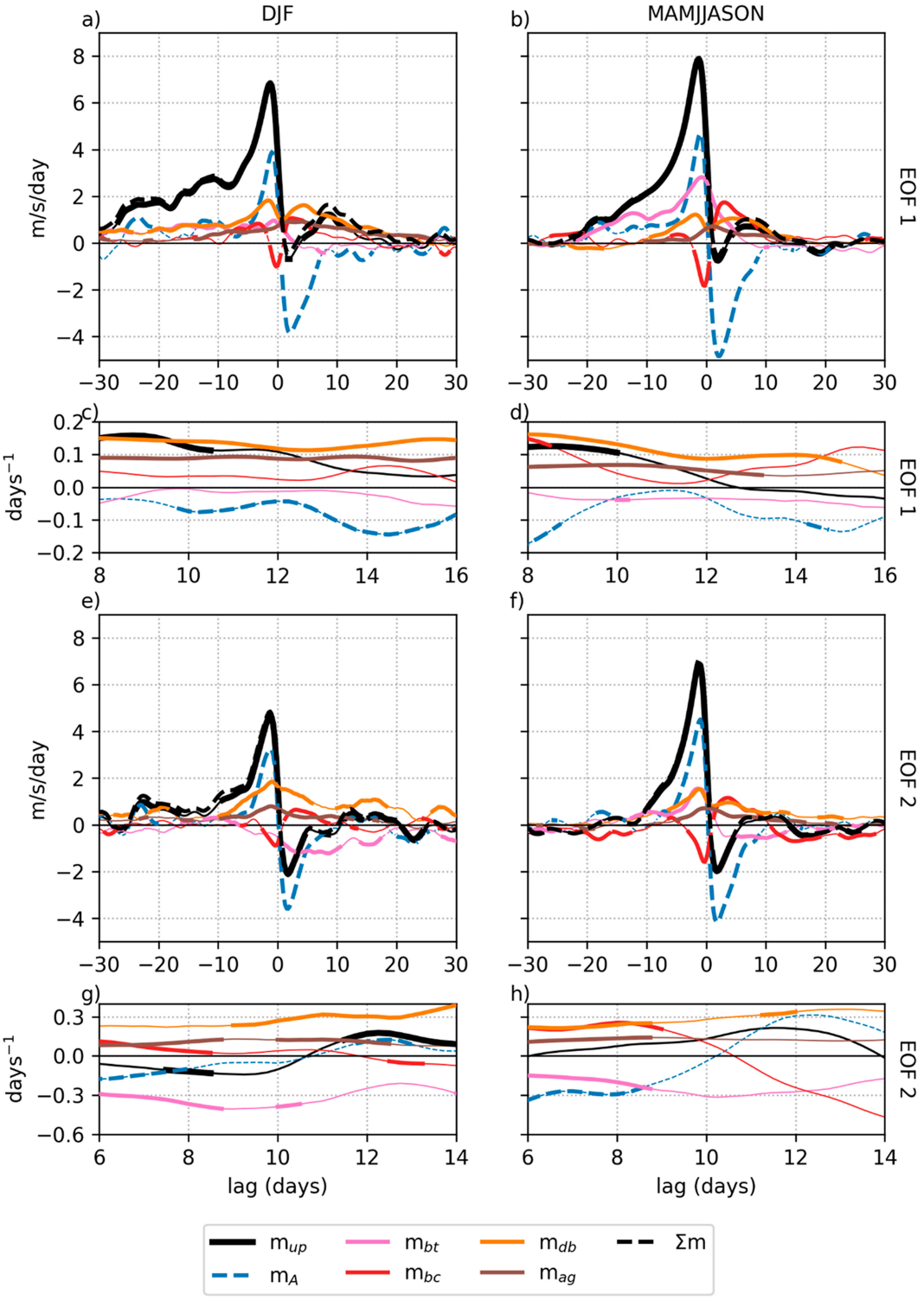

FIG. 3. Partitioning of the upper-level (500–100-hPa) vertically integrated eddy momentum flux convergence (EMFC) as a function of lag in 6-hourly MERRA-2 data for 2005–19 using the wave activity budget [Eq. (9)]. SAM pseudomomentum sources are analyzed separately for (a) DJF and (b) MAMJJASON in EOF1 and (e) DJF and (f) MAMJJASON in EOF2. SAM feedbacks, calculated following N14 (see section 3a), are also shown separately as a function of lag for (c) EOF1 DJF and (d) MAMJJASON and (g) EOF2 DJF and (h) MAMJJASON. m_{up} is the upper-level EMFC projected onto the SAM; m_A are the changes in wave activity (pseudomomentum), which

across the jet (akin to baroclinic injection of momentum), it could induce an EMFC and also reinforce SAM's growth. When the wave activity tendency is nonzero, as it is near lag day 0, it is difficult to determine the exact relationship between EMFC and diabatic pseudomomentum forcing. Furthermore, the diabatic reinforcement of SAM seen here only captures the eddy effect of diabatic heating; lower-level adjustments to baroclinicity by diabatic heating are not its "direct" effects and are not quantified here. Thus, diabatic reinforcement of SAM in MERRA-2 does not imply that the annular mode will be weaker in dry models.

At positive lags, both seasons suggest an eddy–jet feedback, evinced by positive correlations of the EMFC with EOF1 at lag days 8–12 (Lorenz and Hartmann 2001; Simpson et al. 2013) and computed explicitly in Figs. 3c and 3d. The feedback in DJF is larger than in MAMJJASON, which could be attributed to stratospheric influence (Byrne et al. 2016; Saggioro and Shepherd 2019). Another (and not mutually exclusive) possibility is that the propagation in MAMJJASON could be reducing EOF1's persistence relative to DJF (Lubis and Hassanzadeh 2021).

Regardless of the distal cause, the SAM eddy–jet feedback in MERRA-2 is proximately due to diabatic heating and the eddy heat flux (Figs. 3c,d). For the stationary regime, the diabatic term is the largest positive contributor to the budget for lag days 0–20 (Fig. 3a). For the propagating regime, the baroclinic term is the largest positive contributor for lag days 2–4, but it has parity with the diabatic term for lag days 5–15 (Fig. 3b). EOF2 has similar relationships, where the diabatic term is the largest positive term for these lags for the stationary regime, and on par with the baroclinic term for days 0–10 for the propagating regime. Because m_A is statistically indistinguishable from zero during most of this feedback period, we have some confidence here that pseudomomentum injected by diabatic heating is contributing to the positive feedback through the EMFC during this period (Figs. 3a,b,e,f).

A consequence of the importance of diabatic heating is the overestimation of barotropic effects by N14, who implicitly combine the two (cf. supplemental Fig. 2). Figures 3c, 3d, 3g, and 3h show barotropic mixing is a negative feedback on both EOFs in all seasons, suggesting that wave-breaking is acting to return the jet toward its climatological-mean. N14 also neglect ageostrophic effects, but quantifying them reveals their magnitude is about half of the EMFC's at lag days 8–12 for EOF1 (Figs. 3a,b). Interestingly, this implies positive contributions to persistence from ageostrophic eddy fluxes, but deeper investigation of how ageostrophic fluxes might be interacting with SAM in MERRA-2 is left to future work.

To understand cross-EOF interactions, we must determine the period of propagation and choose the (arbitrary) signs for the EOFs. Here, we choose signs such that progression from positive EOF1 to positive EOF2 to negative EOF1 to negative EOF2 represents poleward propagation. The period is about 60 days, determined by compositing the propagation events detected using the scheme outlined in section 3a, whose results are shown in Fig. 4e. The 60-day period suggested by the compositing analysis is supported by a strong peak in the EOF1 power spectrum at around 60 days (not shown), and it is consistent with earlier, observationally based estimates of meridional propagation (Riehl et al. 1950; Feldstein 1998). Thus, where an EOF2 pseudomomentum source is positively correlated with EOF1 within 15 days of EOF1's peak, that pseudomomentum source is contributing to poleward propagation, and similarly for EOF1 pseudomomentum sources negatively correlated with EOF2.

More than 15 days prior to the peak or 15 days after the peak (one-quarter period), negative EOF2 correlations with EOF1 are now consistent with poleward propagation, and again similarly but oppositely with EOF1 pseudomomentum sources. All of this is captured by the gray shaded regions in Figs. 4a–d. Note that the EMFC (black lines in Fig. 4) is roughly consistent with poleward propagation at all lags in both seasons, and m_A is generally statistically insignificant/zero outside lag days −5 to 5. Thus, we expect our analysis to pertain reasonably well to changes in zonal momentum, and not just pseudomomentum alone.

From the budget for cross-EOF interaction, the barotropic term clearly initiates the poleward propagation (pink lines in Figs. 4a–d). This is consistent with the wave-breaking propagation mechanism of Lee et al. (2007) found in an idealized dry model, but, to the best of the authors' knowledge, it has not been confirmed in reanalysis until this work. The barotropic initiation of propagation appears with similar magnitude in both seasons, despite referring to DJF as the "stationary" regime. The composite analysis of propagation events (section 3a) confirms the presence of propagation in DJF with 18 of the 81 middle times being in austral summer.

As previously alluded to, one caveat to this barotropic driving is that the peak day of −2 has a small but significant m_A. Despite this, the agreement with previous findings on the barotropic nature of propagation in idealized models (Lee et al. 2007; Lorenz 2023a) suggests that our interpretation is reasonable. Further, m_{bt} is much larger than m_A, and of the same sign, meaning that any changes in pseudomomentum because of barotropic processes are likely not enough to prevent these processes from also impacting zonal momentum.

Another caveat with the cross-EOF budget is the poor budget closure between lag days −5 and 0 (the black dashed line not matching the solid black line) and more broadly the high degree of noise (weak correlations, insignificance) in the budget. Because m_{bt} is computed residually from Eq. (4), but the

←

contribute to and respond to m_{up} (section 2); m_{bt} is the "barotropic" component of m_{up} driven by irreversible potential vorticity mixing; m_{bc} is the "baroclinic" component of m_{up} from the eddy heat flux convergence (the vertical component of the Eliassen–Palm flux divergence); m_{db} is the "diabatic" component of m_{up} driven by latent and radiative heating; m_{ag} are the ageostrophic contributions to m_{up}; and $\sum m = m_A + m_{\mathrm{bt}} + m_{\mathrm{bc}} + m_{\mathrm{db}} + m_{\mathrm{ag}}$ is the reconstruction of m_{up}, which is frequently indistinguishable from m_{up}. Lines appear thin where the bootstrapped 90% confidence interval contains zero.

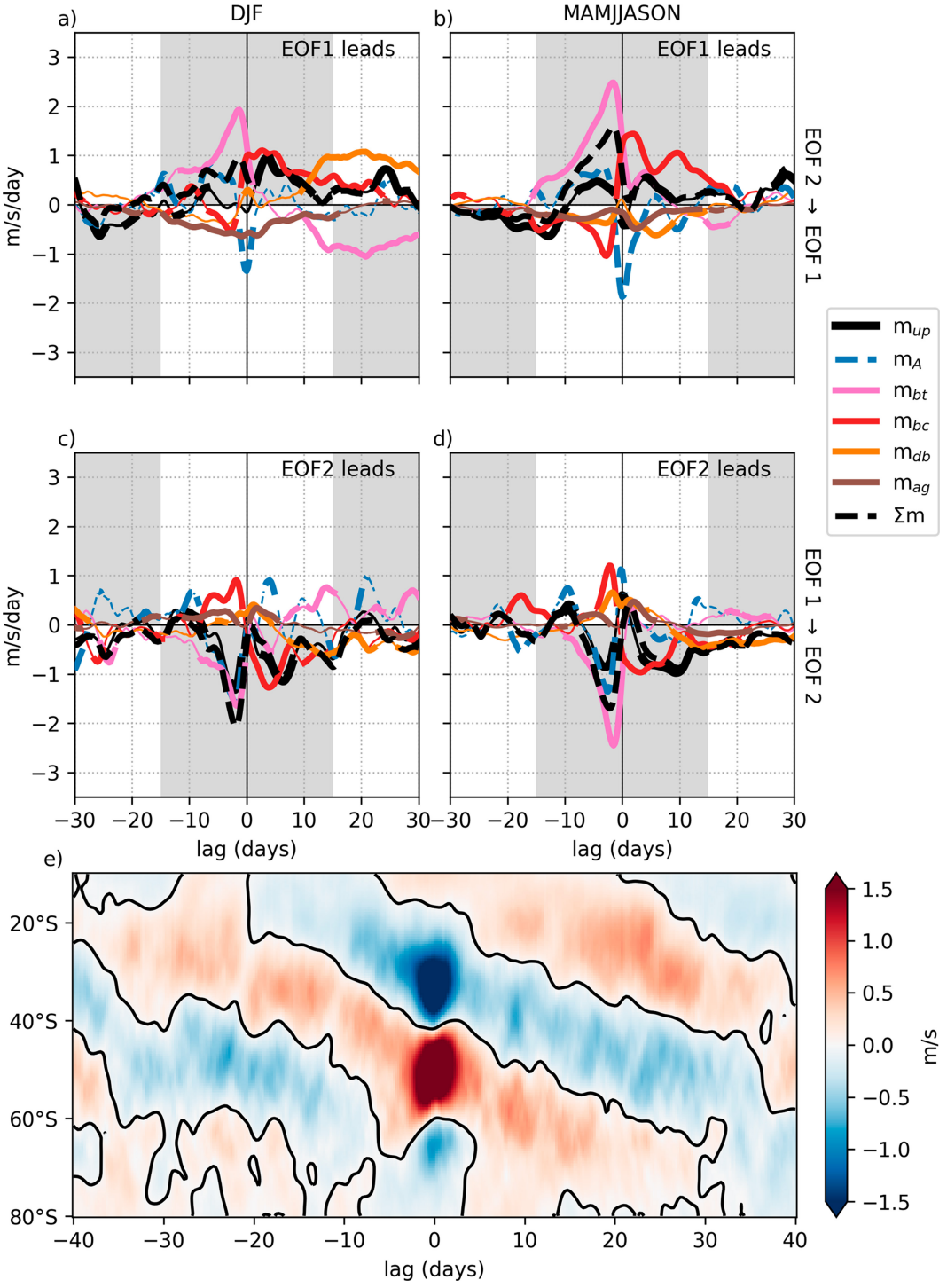

FIG. 4. (a)–(d) As in Fig. 3, but for (a),(b) the EOF2 EMFC partitioning regressed against EOF1 and (c),(d) the EOF1 partitioning regressed onto EOF2 for (a),(c) DJF and (b),(d) MAMJJASON. Gray-shaded regions denote signals of poleward propagation of anomalies (positive EOF1, followed by positive EOF2, followed by negative EOF1, and finally negative EOF2), while white regions denote tendencies toward equatorward propagation. (e) A composite of zonal-mean zonal angular momentum anomalies during 81 propagation events identified using the method outlined in section 3a from MERRA-2 during 2005–19.

sum of all terms relies on Eq. (6), the lack of closure is partially from the EP flux divergence imperfectly balancing the PV flux because of our definition of PV. Thus, part of the error should be equal to the ageostrophic relative vorticity flux ($\overline{v_g'\zeta_a'}$, ζ being relative vorticity), but computing ageostrophic vorticity fluxes accurately is challenging. Our best estimate (not shown) suggests this accounts for at most 50% of the error seen here, the remainder of the error is numerical error related to the computation of wave activity, PV, and their fluxes.

Because of the good closure of the single EOF budgets, as well as some independent checks on the integrity of the budget, we believe this error is generally quite small and not a great cause for concern. The error is relatively more important for the cross-EOF problem due to the weaker signal-to-noise ratio mentioned previously. Overall, this suggests that we may be slightly overestimating the magnitude of the barotropic term, but, given that it is of the right sign and limited to short/fast lags, it is not enough to change our conclusions.

While the propagation is initiated barotropically, it is sustained baroclinically (red lines in Fig. 4). After the barotropic peak for all seasons/EOFs, the baroclinic term becomes the dominant poleward forcing between lag days 1–10. Further, where the eddy heat flux (baroclinic term) is large, the wave activity tendency is generally zero, suggesting that there is baroclinic injection of momentum as a response to the initial anomalies in wave breaking. During the baroclinic response, the barotropic term switches sign, damping the baroclinic response and setting the stage for the next phase of propagation by day 15.

If propagation is initiated barotropically and sustained baroclinically, it is primarily opposed by diabatic heating. Diabatic heating from one EOF is generally the same sign as the prior barotropic and baroclinic peaks, but it peaks after both (day 15–20, orange lines in Fig. 4). Thus, diabatic pseudomomentum forcing appears in quadrature with the EMFC anomalies, increasing persistence rather than furthering propagation, consistent with the separate EOF budgets (Fig. 3). Interestingly, most of this equatorward forcing from diabatic heating comes from the latent heating (see supplemental Fig. 4). This diabatic drag on propagation is strongest in the stationary regime where propagation is weakest (Fig. 4a), where the diabatic feedback on EOFs 1 and 2 is also strongest (Figs. 3a,c). Ageostrophic momentum also appears to oppose propagation (brown lines in Fig. 4), suggesting that the slower response of both ageostrophic and diabatic processes to zonal wind anomalies favors slower propagation and enhanced persistence.

Diabatic opposition to propagation is consistent with a recently performed series of cloud-locking experiments designed to evaluate the role of CRE for the SAM (Lu et al. 2024, manuscript submitted to *J. Geophys. Res. Atmos.*, hereafter L24). In these atmosphere-only GCM experiments, disrupting CRE-circulation feedbacks increases the robustness of propagation and makes the SAM less persistent, supporting the overall interpretations of the pseudomomentum budgets analyzed here in reanalysis. Overall, we have some confidence that the mechanisms depicted in idealized and realistic modeling studies are realized in reanalysis as well–a barotropic initiation of propagation, a baroclinic maintenance, and a diabatic opposition.

To gain more physical insight, we now examine where these pseudomomentum forcings are operating (Fig. 5). At a 10-day lag, the DJF EMFC associated with EOF1 (solid black line in Fig. 5a) retains an EOF1-like pattern (thick gray line), consistent with an overall positive feedback. Diabatic contributions to the positive feedback are concentrated poleward of the jet, decelerating the zonal wind there during the equatorward phase of SAM (positive EOF1) through anomalous pseudomomentum absorption (orange line). Baroclinic pseudomomentum generation (red line) is the dominant term equatorward of the jet for EOF1, appearing on the poleward edge of the equatorward EMFC peak, consistent with an enhanced baroclinic injection with an equatorward shift of the storm tracks.

Looking at EOF2, the DJF EMFC has flipped to a negative EOF2 pattern at a 10-day lag, consistent with the absence of both propagation and a positive feedback (Fig. 5c). Diabatic FAWA sources are again decelerating zonal wind poleward of the jet. Baroclinic processes (red line) are also concentrated poleward of the jet but further poleward than for EOF1 (Fig. 5a). However, these diabatic and baroclinic sources are largely balanced by a growth in wave activity on the poleward jet flank (dashed blue line in Fig. 5c), which complicates the interpretation. The negative EOF2 pattern of the EMFC appears to be generated most strongly by the barotropic piece, with weakened (more positive) dissipation at both flanks of the jet and stronger (more negative) dissipation at the jet core, consistent with the barotropic term as the main negative feedback (Fig. 3g).

For the propagating regime at a 10-day lag, we see evidence of propagation in the EMFC, as expected, with diabatic and baroclinic processes contributing in similar regions as in the stationary regime (Figs. 5b,d). The baroclinic term is shifted slightly further poleward for EOF1 than in DJF, resulting in a positive EOF2-like pattern (Fig. 5b). This shifting of the eddy heat flux, combined with stronger diabatic destruction of FAWA equatorward of the jet and weaker (more positive) dissipation poleward of the jet, results in an overall weaker positive EOF1 pattern for the EMFC (black line) and thus a weaker feedback than for DJF. The barotropic term has a negative EOF1-like response on the poleward edge of the positive EOF2-like baroclinic response, consistent with the barotropically initiated–baroclinically sustained pattern for propagation.

The EOF2 EMFC during MAMJJASON (Fig. 5d) shows a clear negative EOF1 pattern (cf. gray shading in Fig. 5b) at a 10-day lag, again evidence of poleward propagation. Despite this, the diabatic, barotropic, and baroclinic terms largely resemble the stationary regime. The barotropic term is a negative EOF2-like response, in quadrature with the EMFC and consistent with its initiation of propagation. The primary difference between DJF and MAMJJASON now comes from the wave activity growth (more negative) in the subtropics in MAMJJASON rather than near the pole in DJF. This highlights the careful synchronization between diabatic heating, upper-level wave growth, and lower-level eddy-heat flux required for propagation (Lee et al. 2007). Diabatic contributions are further examined in section 4b.

b. SAM diabatic pseudomomentum sources

As discussed in section 2, the diabatic pseudomomentum forcing can be separately decomposed into contributions from latent heating, long- and short-wave clear-sky radiative heating,

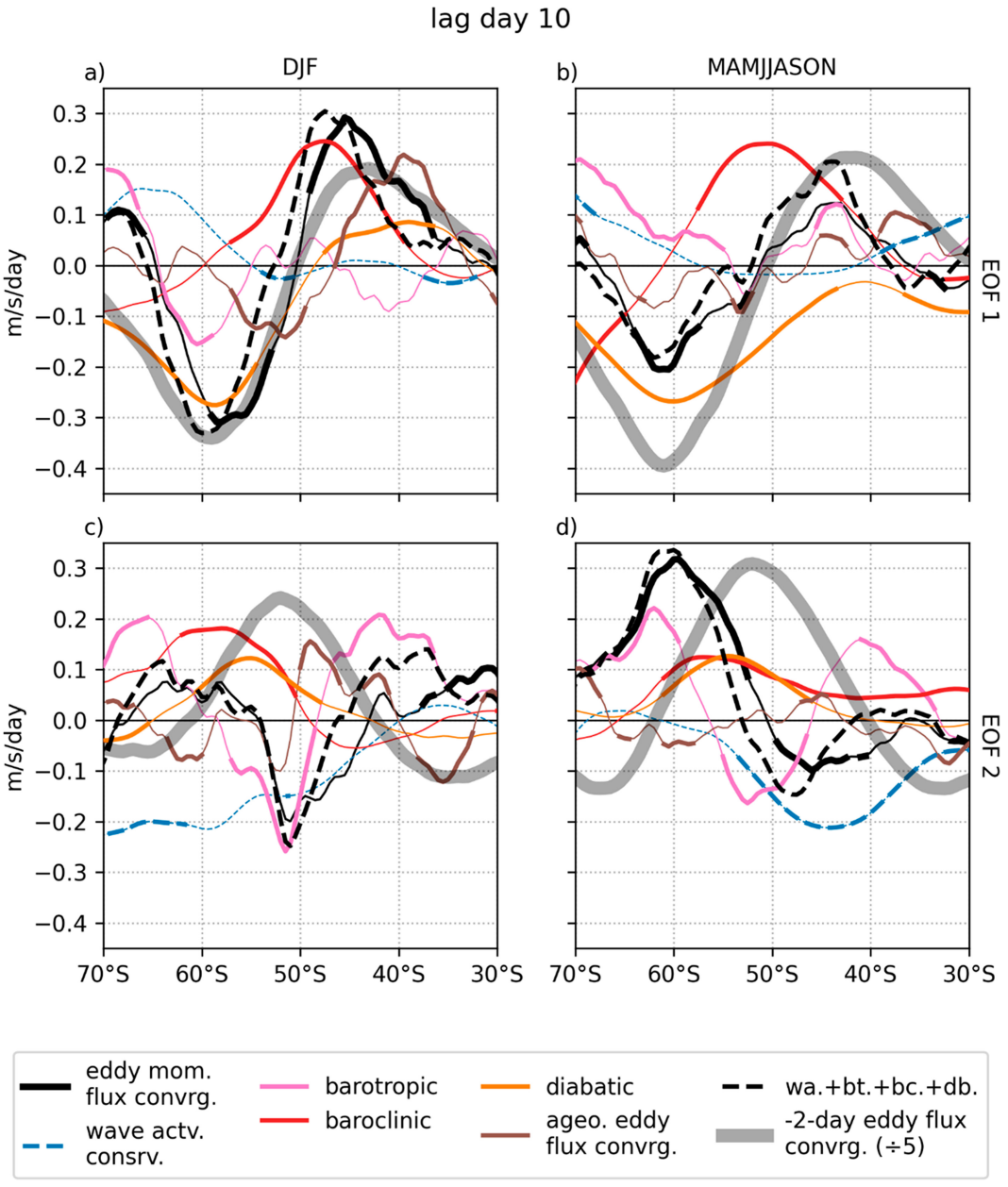

FIG. 5. The EMFC partitioning depicted in Fig. 3, now latitudinally varying by regressing onto EOF1 for (a) DJF and (b) MAMJJASON and onto EOF2 for (c) DJF and (d) MAMJJASON at a 10-day lag. For reference, the thick gray line shows the peak EMFC at peak day (−2), reduced in magnitude by one-fifth. As before, lines appear thin where the bootstrapped 90% confidence interval contains zero.

long- and short-wave cloud radiative heating, and turbulent heat diffusion. Shortwave contributions (shown in supplemental Fig. 3) are found to be generally opposing longwave contributions, but they are an order of magnitude smaller. The turbulent heat diffusion in the upper-troposphere is also an order of magnitude smaller than the other terms (not shown). Thus, while included in the total contributions, we neglect these for the remainder of this analysis.

The resulting decomposition reveals different processes dominate at different time scales (Fig. 6). On short time scales less than ±10 days, latent heating is generally the largest positive contributor to SAM among the diabatic terms (solid teal lines in Fig. 6), except for EOF2 during DJF. In general, much of the temporal structure of the diabatic pseudomomentum forcing comes from the latent heating. Consistent with Lutsko and Hell (2021), we find latent heating is a positive feedback on SAM persistence (Figs. 6c,d,h). While this may seem at odds with Xia and Chang (2014), who argue for a negative latent heating feedback through a reduction in baroclinicity, our framework includes adjustments of low-level

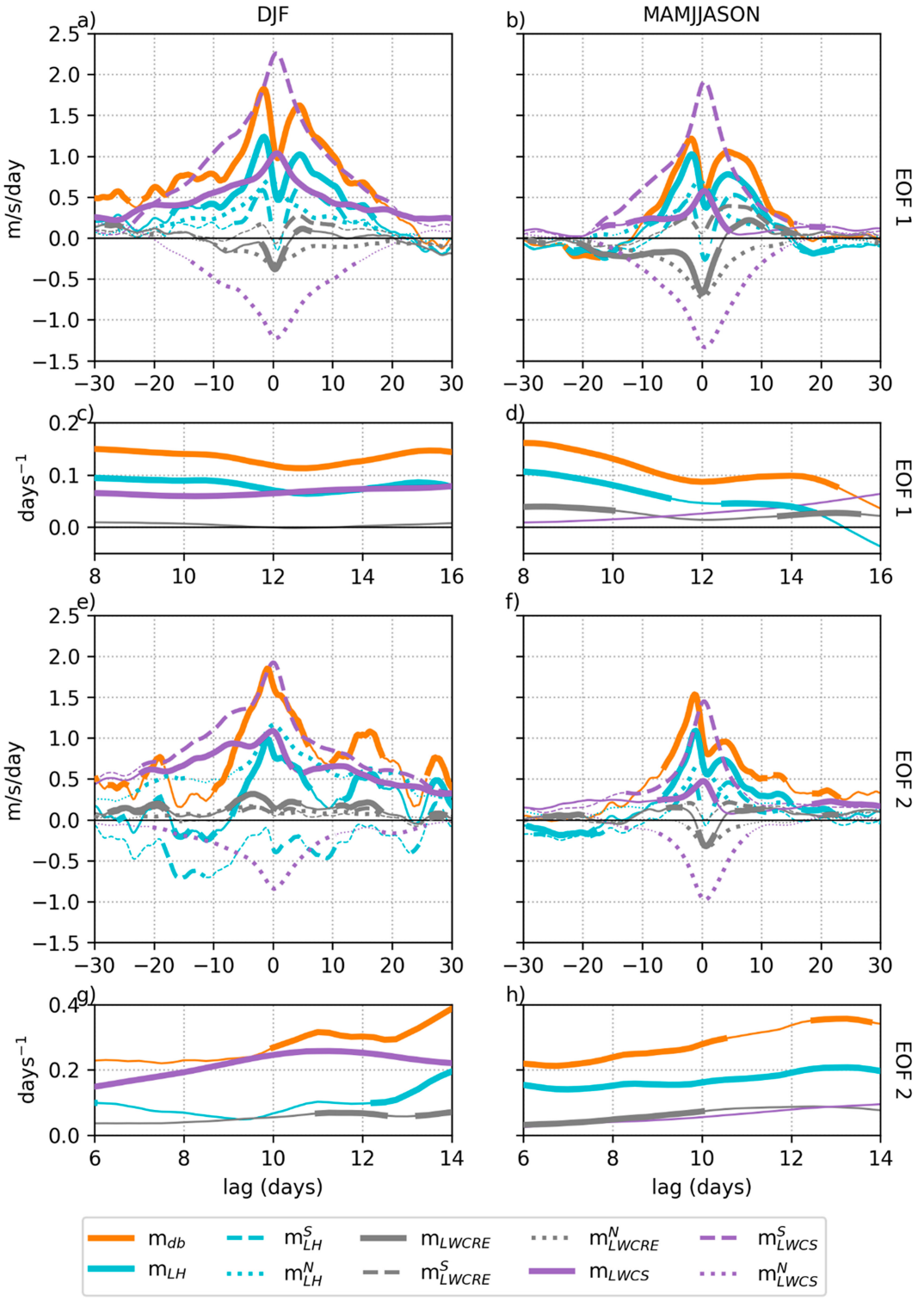

FIG. 6. As in Fig. 3, but the upper-level contributions to the pseudomomentum forcing from different diabatic processes [Eq. (10)]. m_{db} is the same diabatic component of m_{up} as in Fig. 3, m_{LH} is the component of m_{up} driven by latent heat release, m_{LWCRE} is the component of m_{up} driven by longwave (LW) cloud radiative heating (all-sky minus clear-sky), and m_{LWCS} is the component of m_{up} driven by LW clear-sky radiative heating. Shortwave cloud and clear-sky cooling are included in m_{db}, but they are left for supplemental Fig. 3 as they are negligible. Also shown separately are contributions from anticyclonic (southward) wave breaking (superscript *S*) and cyclonic (northward) wave breaking (superscript *N*).

baroclinicity (even by diabatic heating) in the baroclinic term rather than in the diabatic one, as lower-tropospheric diabatic heating functions mainly to reduce the heat flux into the upper troposphere.

While the role of latent heating is generally consistent across regimes, clear-sky forcing of pseudomomentum primarily explains the difference between stationary and propagating regimes (solid purple lines in Fig. 6). The clear-sky forcing is exclusively positive, with a magnitude ranging from 2 to 5 times larger during DJF than during MAMJJASON (Fig. 6). Because clear-sky contributions are the dominant diabatic contributions beyond lag day 10 in DJF (Fig. 6a), and because diabatic terms are the largest positive contributions for the entire budget (Fig. 3a), clear-sky heating explains much of the increased persistence of the stationary regime (Figs. 6c,h versus Figs. 6d,g).

While clear-sky and latent heating dominate at their respective time scales, cloud radiative heating is a second-order contributor to SAM dynamics (solid gray lines in Fig. 6). Given the relatively weak cloud response and complex vertical structure of the cloud heating (Li and Thompson 2016), this is unsurprising. However, despite being a small pseudomomentum source, it is the only term to clearly change sign over time in EOF1. At leads −10 to around lag day 2, cloud contributions are negative, but after lag day 3, the cloud contributions are positive, peaking around lag days 5–8 and weakly increasing SAM persistence (Figs. 6b,d). This may partially explain the challenge in diagnosing cloud impacts.

Further breaking the pseudomomentum forcings into separate contributions from cyclonic and anticyclonic waves, nearly all the positive forcing comes from (upper-level) anticyclonic waves (dashed lines in Fig. 6). Radiative heating within cyclonic waves opposes SAM in all seasons for all EOFs (dotted purple and gray lines). For clear-sky heating, the total contributions result from a large compensation between anticyclonic contributions, peaking between 1.5 and 2.2 m s^{-1} day^{-1}, and cyclonic contributions, peaking between 0.8 and 1.3 m s^{-1} day^{-1}. One explanation for this result may be that radiative heating is strengthening both cyclonic waves on one flank of the jet and anticyclonic waves on the opposite flank, resulting in competing effects.

To test this hypothesis and gain more insight into how diabatic heating modulates wave activity and momentum, we again analyze the response's spatial pattern. Adding the vertical dimension, we see that diabatic pseudomomentum forcing for EOF1 is not only concentrated poleward of the jet, but also below 300 hPa (Fig. 7). For the stationary regime, latent heating broadly reinforces the peak-day EMFC anomaly (contour lines), in-phase with the anomaly on both flanks of the jet and still at nearly a third of the magnitude of the peak EMFC ten days later (Fig. 7a). This is likely from an equatorward shift of the storm tracks, as we show in section 4c. During the propagating regime, latent heating is also in-phase around 500 hPa poleward of the jet, somewhat weaker than during the stationary regime (Fig. 7b).

The radiative contributions from cloud and clear-sky heating are less in-phase with the EMFC anomalies than latent heating, and they are mostly concentrated below 200 hPa. Cloud radiative heating is weakly in-phase with EMFC anomalies poleward of the jet for both seasons (Figs. 7c,d). Cloud contributions have the most vertical variation of the diabatic terms, which is significant because the net impact results from a vertical average. Because there is great uncertainty in SAM's influence of the vertical profile of cloud heating (Li and Thompson 2016), their small magnitude identified in MERRA-2 may not be reproduced by other reanalyses or models.

Clear-sky pseudomomentum sources exhibit the most variation of all the diabatic sources for EOF1 (Figs. 7e,f). Clear-sky forcing during the stationary regime is well-aligned with the EMFC anomalies, acting to decelerate the zonal wind poleward of the jet throughout the entire upper troposphere (Fig. 7e). [We can reasonably attribute this pseudomomentum forcing to a momentum forcing since $m_A \approx 0$ at lag day 10 (Fig. 3c).] In contrast, the propagating regime exhibits approximately 50% weaker clear-sky influence and is generally less in-phase with the EMFC poleward of 50°S (Fig. 7f). This result could support proposals for a stratospheric influence on EOF1 during DJF (Byrne et al. 2016; Saggioro and Shepherd 2019), if stratospheric temperature anomalies are modifying upper-tropospheric longwave radiation. Further investigation for a radiative pathway for stratospheric influence is left for future work.

When looking at the spatial structure of diabatically forced contributions to EOF2 pseudomomentum, we see mostly reinforcement of the EOF2 EMFC pattern at a 10-day lag (Fig. 8). This is particularly the case for latent and cloud radiative heating, which reinforce the stronger jet in the midtroposphere in all seasons (Figs. 8a–d). In both seasons, the cloud contributions to EOF2 (Fig. 8c,d) are mostly opposite sign to their EOF1 contributions (Figs. 7c,d), still exhibiting the most cancellation in the vertical mean. Clear-sky heating projects weakly onto EOF2, largely within −0.1 to 0.1 m s^{-1} day^{-1}. During the propagating regime, clear-sky contributions (Fig. 8f) are a weak negative EOF1-like pattern (cf. Fig. 7f), but this only weakly supports propagation (supplemental Figs. 4b,d).

c. *Analysis of large breaking waves*

The final part of this analysis identifies regions of large, nonlinear, upper-level cyclonic and anticyclonic waves to detect consistent trends between physical drivers of diabatic heating and its impact on pseudomomentum. We do this by averaging different fields over the same domain as the upper-level waves, and regressing them against equatorward SAM (EOF1) as described in section 3b. By examining both the sign of the climatology of these fields and the sign and significance of their response to SAM, we reveal probable mechanisms through which changes in jet latitude might lead to the diabatic feedbacks previously discussed.

We focus on regions of large wave activity for two reasons. First, large FAWA centers should have an outsized impact on the wave activity budget, and thus on zonal momentum, and they should behave similarly to smaller FAWA regions as FAWA does not distinguish between wave types or numbers. Second, we expect that waves in the early stages of breaking should be the largest contributors to wave activity (Nakamura and Huang 2017), which we separately confirm with over 90% of these large-amplitude waves exhibiting overturned PV contours (see supplemental Figs. 5 and 6). Because wave breaking is

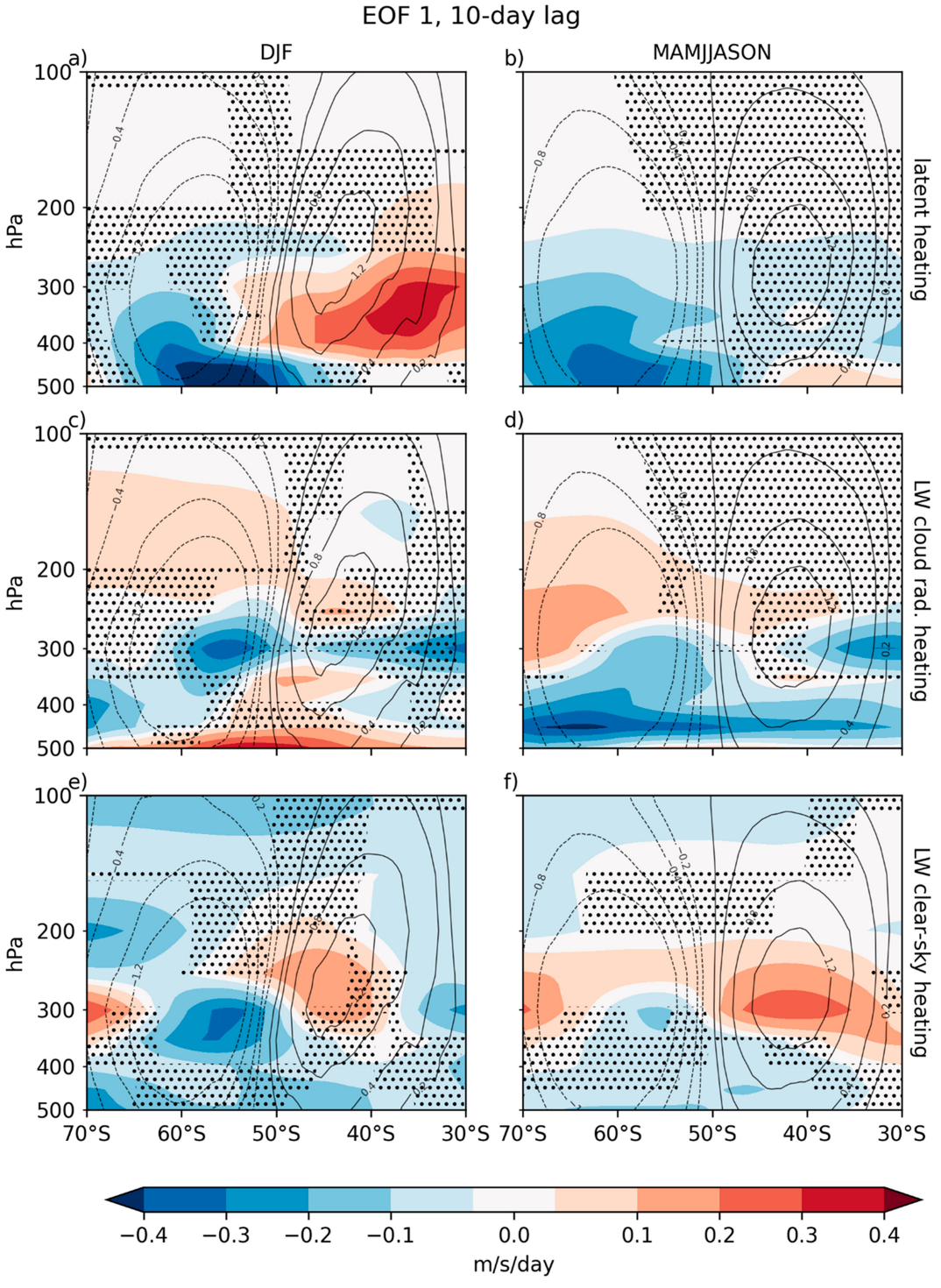

FIG. 7. The diabatic contributions to SAM pseudomomentum depicted in Fig. 6, regressed onto the EOF1 index at a 10-day lag (shading). Contributions are shown from (a),(b) latent heating (m_{LH}); (c),(d) cloud longwave heating (m_{LWCRE}); and (e),(f) clear-sky longwave heating (m_{LWCS}) for DJF and MAMJJASON, respectively. Contours are the eddy momentum flux convergence at day −2 (in m s^{-1} day^{-1}) for reference. Stippling represents regions where bootstrapped 90% confidence intervals contain zero.

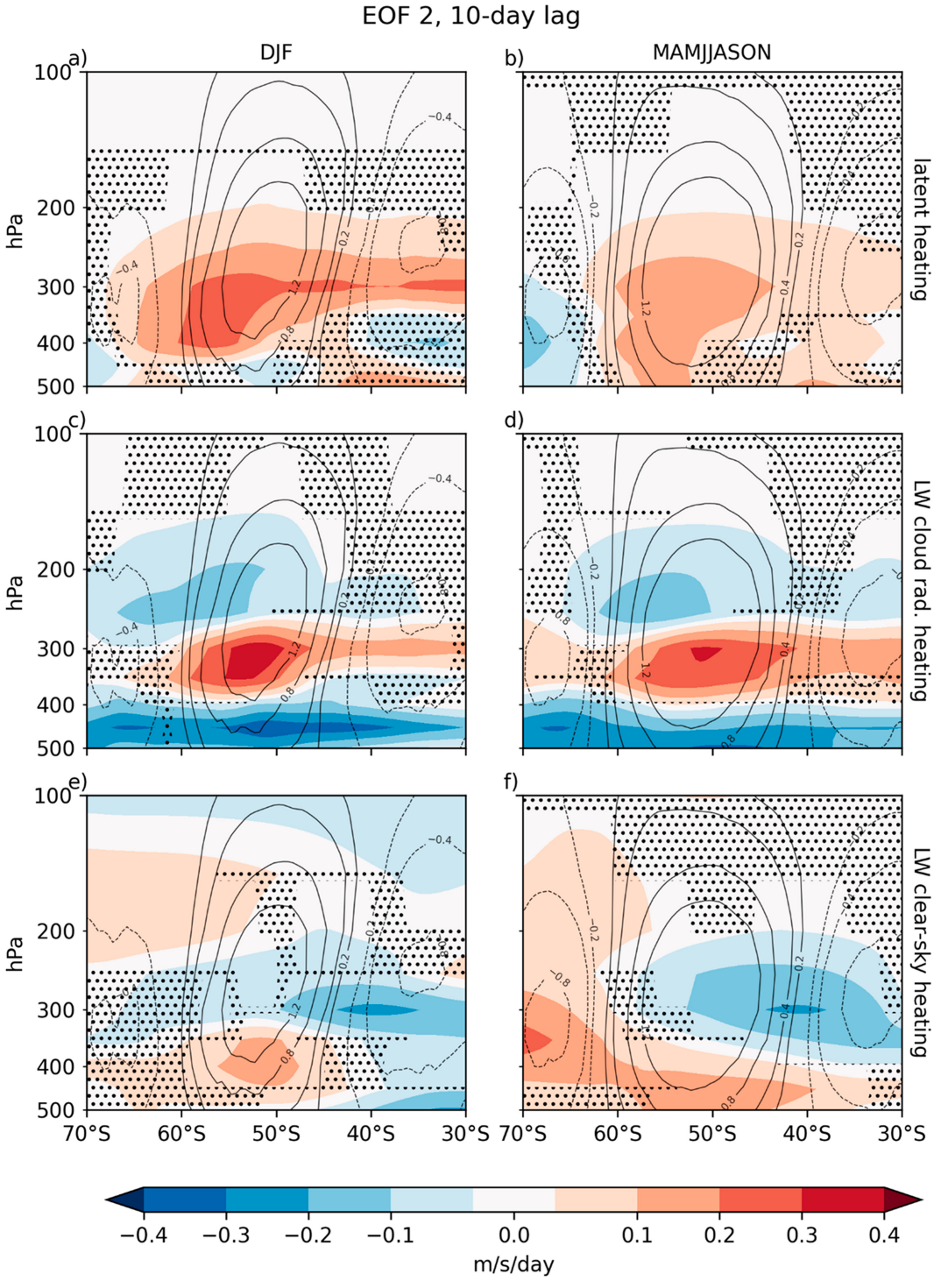

FIG. 8. As in Fig. 7, but regressed against the EOF2 index.

known to play an important role in the life cycle of SAM's generation and feedbacks (Thompson and Wallace 2000; Barnes et al. 2010), our analysis of these cyclonic breaking waves (CBW) and anticyclonic breaking waves (ABW) should help connect changes in diabatic heating to their influence on SAM's dynamics.

We examine the 10-day lag correlations between EOF1 and the wave-averaged fields for year-round data, separating waves into those poleward of the jet (50°–70°S) and equatorward of the jet (30°–50°S). We make this distinction for two reasons. First and foremost, the EMFC has different signs on

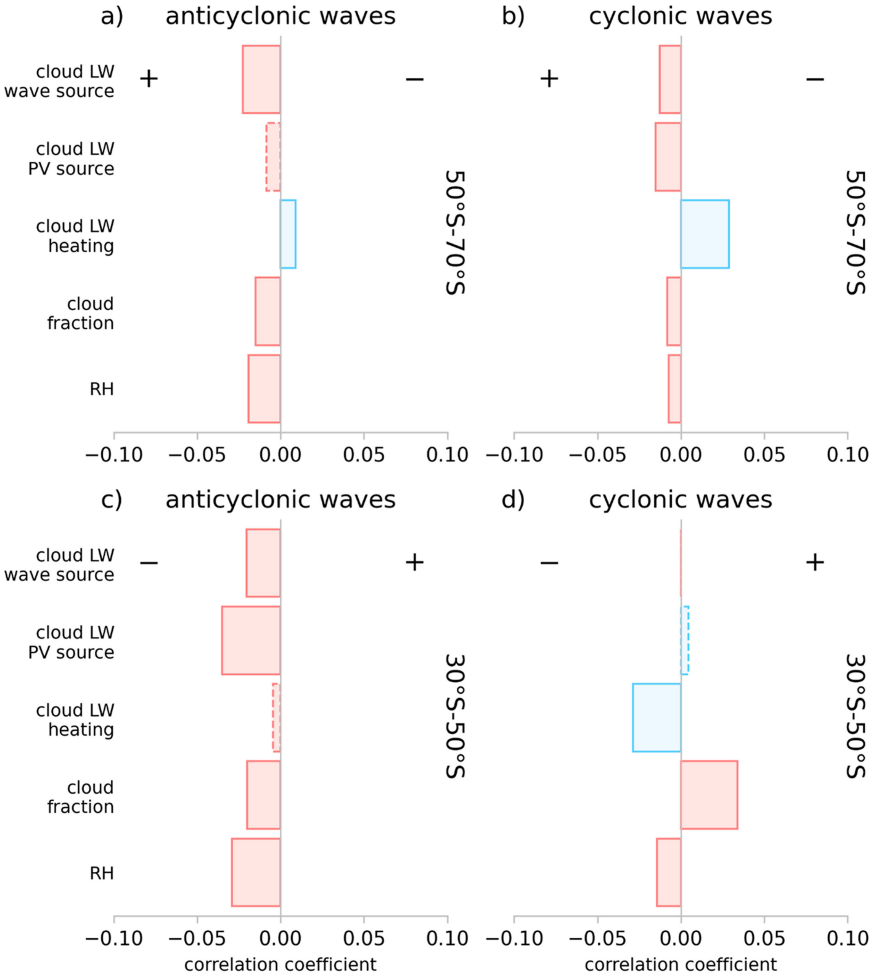

FIG. 9. Correlation coefficients of EOF1 with the 10-day-lagged, 500–100-hPa-averaged, year-round relative humidity, cloud fraction, longwave cloud heating, the longwave cloud heating PV source, and the longwave cloud forcing of wave activity ("wave source") for (a) anticyclonic wave regions between 50° and 70°S, (b) cyclonic wave regions between 50° and 70°S, (c) anticyclonic wave regions between 30° and 50°S, and (d) cyclonic wave regions between 30° and 50°S. Blue shading indicates that the mean value of the field for each composite region is negative; red shading indicates the mean value is positive. Signs are chosen for the PV source fields to match the sign of the PV anomaly, i.e., a positively correlated PV source for anticyclonic waves corresponds to anticyclonic strengthening, whereas a positively correlated source for cyclonic waves corresponds to cyclonic strengthening. The wave activity signs should be interpreted in the same manner, following the sign conventions discussed in section 2. Plus and minus signs by the wave activity source correlations indicate whether the changes are same-signed (+) or opposite-signed (−) as the SAM momentum anomalies (i.e., either a positive or a negative feedback). Dashed outlines are not significant correlations at the 95% confidence level.

opposite sides of the jet (approximately 50°S), and so a positive diabatic wave forcing may reinforce or oppose this pattern depending on its latitude (as suggested by the plus/minus signs in Figs. 9–11, assuming it propagates away from its source). Second, the distributions of these fields are quasi-bimodal, and they are more Gaussian if first separated by latitude (not shown). The latitudinal distribution of waves is shown in supplemental Fig. 7.

As may be expected, the cloud-related fields suggest that the moisture and temperature anomalies associated with SAM may be responsible for producing the diabatic heating changes which lead to the feedback. Consistent with Fig. 7d, the positive longwave (LW) cloud feedback is primarily coming from decreases in the cloud pseudomomentum sources in both poleward ABW (PABW) regions and poleward CBW (PCBW) regions (Figs. 9a,b). This decreased wave source is accompanied by a consistent weakening of upper-level cloud LW cooling in both regions, along with decreases in upper-level relative humidity and cloud fraction. Physically, this suggests this diabatic feedback may be due to a reduced cloud

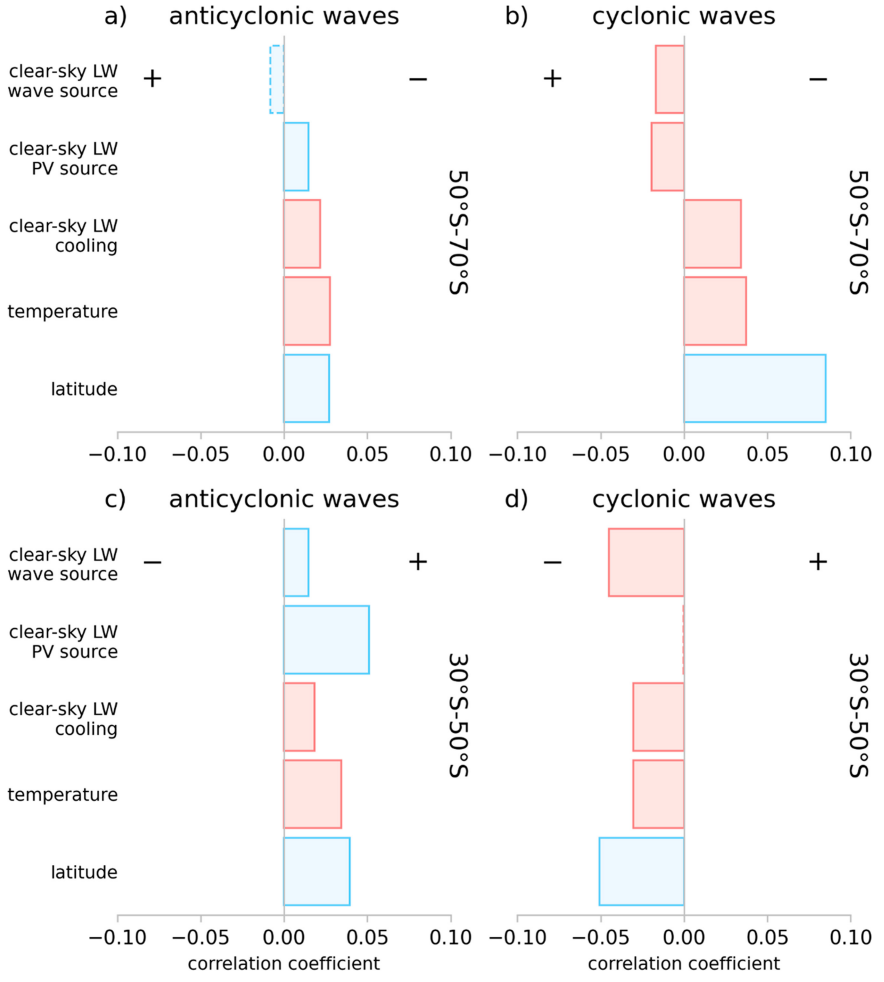

FIG. 10. As in Fig. 9, but for 500–100-hPa centroid latitude, temperature, longwave clear-sky cooling (negative heating), longwave clear-sky PV source, and longwave clear-sky wave activity source. The sign convention for PV sources and wave sources is as in Fig. 9.

fraction resulting from an upper-level reduction in relative humidity in response to the more equatorward jet.

The effects of heating on PV depend on the vertical profile of the heating [cf. Eq. (5)], and so changes (or lack thereof) in the vertically averaged heating do not directly imply changes in PV. Even so, there is a reduction of the cloud cyclonic PV generation for PCBW (Fig. 9b) and a weak decrease in the cloud anticyclonic PV source for PABW (Fig. 9a), which we might expect given that cloud LW cooling weakens similarly in both regions. Note that the PV tendency is scaled to have the same sign as the PV anomaly to emphasize the local impact on the wave and to avoid confusion from the sign dependence of PV anomalies on the Coriolis parameter.

Looking at equatorward ABW (EABW), we see a nearly identical pattern to PABW regions (Fig. 9c), except that the weakened cloud forcing of pseudomomentum is a negative feedback in this region. There are no significant changes to the dynamical measures in equatorward CBW (ECBW) regions as well, though we do see a robust increase in cloud LW cooling coincident with increased cloud fraction, opposite the response in poleward regions (Fig. 9d). Given the negative, anomalous cloud pseudomomentum forcing between 30° and 50°S in Fig. 7d, it is likely there is a weak negative feedback in the equatorward regions that is difficult to identify amidst the noise. However, the wave activity budget (Fig. 6b) shows this negative feedback in equatorward regions is weaker than the positive one in poleward regions.

Poleward of the jet, changes in pseudomomentum from clear-sky heating are also a positive feedback, where an equatorward jet is linked to more equatorward and thus warmer waves for PABW, PCBW, and EABW regions (Figs. 10a–c). The warmer temperatures coincide with increased longwave cooling (negative heating) in all these regions, as well as a weakening of both anticyclonic PV damping (less negative) and cyclonic PV generation (less positive) (Figs. 10a–c). This suggests the positive clear-sky feedback comes from the equatorward shift of the storm tracks, producing warmer waves with increased longwave cooling in poleward waves, strengthening ABW and weakening CBW.

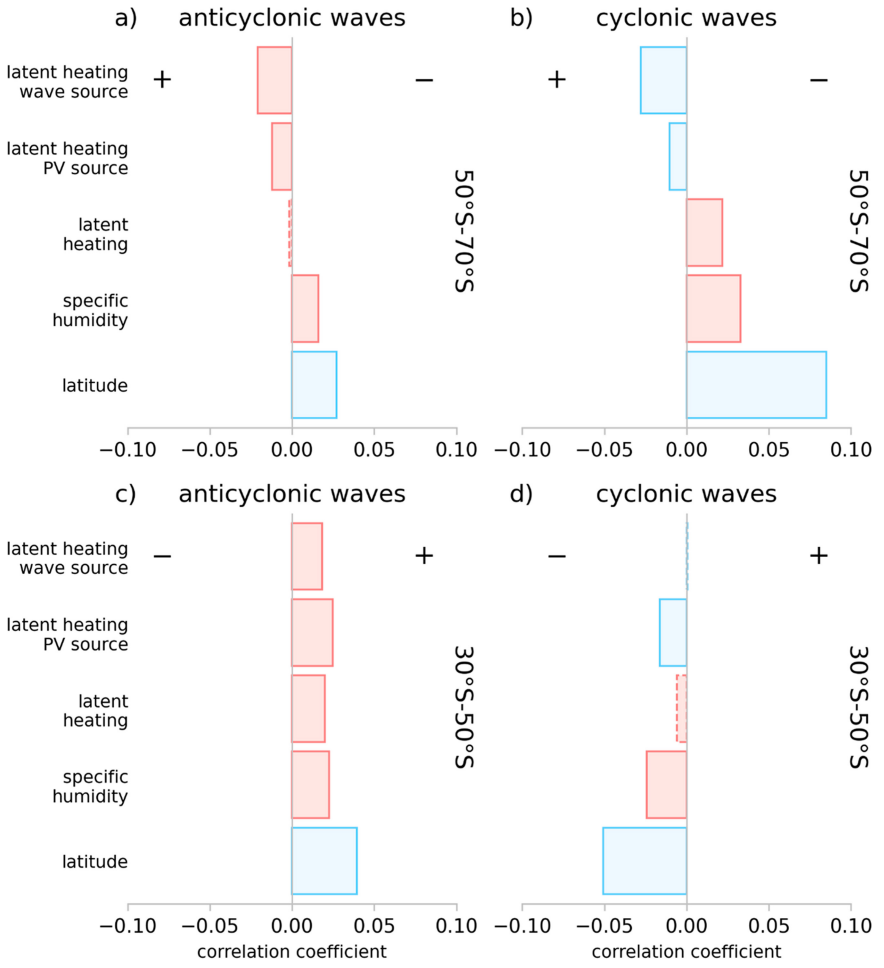

FIG. 11. As in Fig. 9, but for 500–100-hPa centroid latitude, specific humidity, latent heating tendency, latent heating potential vorticity source, and latent heating forcing of pseudomomentum.

Interestingly, ECBW shows opposite trends to the other regions (Fig. 10d). Here, we see a decrease in the pseudomomentum source, implying a negative feedback. This is consistent with a counterintuitive shift toward higher latitude CBW (during equatorward SAM), a reduction in temperature, and a weakening of clear-sky cooling (Fig. 10d). However, our previous results suggest that SAM's clear-sky heating acts as a positive feedback equatorward of the jet (Figs. 6b and 7f), so this negative feedback would imply that the changes in EABW outweigh this.

To conclude this analysis, we examine fields relevant to latent heating, which also suggest the positive feedback is due to the shift in storm tracks (Fig. 11). As with the clear-sky fields, the equatorward shift in cyclones and anticyclones result in more moisture availability and stronger latent heating in PABW, PCBW, and EABW regions (Figs. 11a–c). Where the latent heating increase is robust, it strengthens EABW and weakens PCBW, injecting pseudomomentum equatorward of the jet and removing it on the poleward flank, thus acting as a positive feedback. These results are consistent with Figs. 6b and 7b, as well as with observational studies finding that latent heating increases the persistence of the North Atlantic storm track (Woollings et al. 2016). The most robust changes are seen for PCBW, where cyclones shift more equatorward, and thus have more moisture available for latent heating (Fig. 11b).

Like the clear-sky response, the pattern is reversed for ECBW regions: more poleward cyclones, with less moisture available and mildly weaker latent heating (Fig. 11d). While the changes to CBW equatorward of the jet during SAM are not consistent with the other regions, they are internally consistent, suggesting that this analysis does identify the relevant physical mechanisms which are mediating the diabatic feedbacks on SAM. Thus, 10 days after peak equatorward SAM, storm tracks are still displaced, increasing the latent heating and clear-sky radiative cooling poleward of the jet, damping upper-level waves on its poleward flank, fluxing momentum equatorward, and enhancing SAM's persistence.

5. Conclusions

To quantify the contributions of diabatic, barotropic, and baroclinic processes to the persistence and propagation of

SAM, we have examined a detailed partitioning of the EMFC in MERRA-2 from 2005 to 2019 using the finite-amplitude wave activity framework. Principally, we find that diabatic heating, particularly from latent and longwave clear-sky heating, is the dominant pseudomomentum source at positive lags during DJF, for both the jet shift (EOF1) and jet pulsing (EOF2) modes of variability. Thus, diabatic effects constitute the largest eddy–jet feedback for the stationary regime of SAM variability. This is a novel contribution of this work which corrects the earlier work of N14.

Because diabatic heating is the largest feedback during DJF, and because this feedback is tied to the latitude of wave breaking and thus the jet itself, efforts to improve representation of SAM in models should first consider the climatological jet latitude. However, improved climatological jet latitudes have not eliminated DJF time scale biases in CMIP6 (Bracegirdle et al. 2020), and these results urge further consideration of whether the often-parameterized diabatic processes in models generate a realistic vertical profile of heating in response to SAM.

We emphasize that the presence of a positive feedback from latent heating in reanalysis does not imply that dry models should have shorter SAM time scales. Because of the tight coupling between the eddy–mean flow interactions that govern the annular mode's evolution, removing one process (such as latent heating) has too many compounding effects to suggest a linear response of SAM's time scale. However, our results do suggest caution when generalizing findings from idealized, dry models commonly utilized to study annular mode dynamics to findings about the real atmosphere.

For the propagating regime of SAM variability during March–November, we find baroclinic contributions from the meridional eddy heat flux are the largest pseudomomentum source for EOF1 and EOF2 at positive lags, followed closely by diabatic heating. Additionally, barotropic contributions initiate the EOF1-EOF2 interaction which drives poleward propagation, which is supported by a baroclinic response. Diabatic heating generally opposes poleward propagation, consistent with the finding that it increases persistence (Lubis and Hassanzadeh 2021; L24).

Additionally, diabatic heating may explain the tendency toward a stationary regime in DJF through a stronger clear-sky pseudomomentum source and a stronger damping of propagation than in MAMJJASON. More fundamentally, the tendency toward propagation or nonpropagation has been explained as result of double or single jet states (Lee et al. 2007), the latter being more common in summer due to the weakened eddy-driven jet. These mechanisms are not mutually exclusive—jet latitude and strength have important influences on diabatic heating. These results for the propagating regime highlight the careful orchestration between processes required to produce an accurate SAM time scale and thus to predict SAM evolution. Future progress relies on identifying the controls on the speed of propagation and partitioning the EMFC in full-physics models.

In tandem with this work, some of the authors have partitioned the SAM EMFC in a suite of "cloud-locking" experiments in the Exascale Energy Earth System Model (E3SM) designed to eliminate cloud–circulation feedbacks (L24). L24 also utilize the wave activity framework to explain how CRE produces a positive feedback to SAM in E3SM, in part by disrupting propagation in a manner consistent to the findings of this work for MERRA-2.

While we contend that the strong agreement between the model-based work of L24 and this work should give some confidence in these results, we emphasize that the computation of diabatic wave activity sources performed here is novel to this work, and there is limited ability to constrain the magnitudes of these sources. Because some portion of the wave activity budget must always be calculated residually, the closure of our budgets can only partially assess any error in our diagnostics. To combat this, we have tried to develop some theoretical expectations of its magnitude in the supplemental material, and to contextualize our work with the existing literature as much as possible. Given the consistencies between our work and many other model-based works, as well as some aspects of the independent work of N14 (supplemental Fig. 2), we have confidence that the significance of diabatic heating found here is robust to any unquantifiable remaining error.

A final caveat is suggested by the results of Chemke and Polvani (2019), who argue that discrepancies between reanalyses and models sometimes represent deficiencies in the reanalyses and not the models, as in the case of trends in Hadley cell strength. While this analysis cannot definitively demonstrate the validity of these results beyond MERRA-2, this work is internally consistent and broadly in agreement with modeling studies, suggesting that our key findings on the importance of diabatic heating for SAM are likely not a result of artifacts in MERRA-2.

Our approach taken here elucidates many different facets controlling the variability of the Southern Hemisphere zonal wind. We find diabatic heating is crucial to setting the time scale of a largely barotropic phenomena. We also find consistencies between reanalysis and idealized modeling studies, increasing our confidence that mechanisms operating in the idealized studies are also operating in the real atmosphere. We contend that coupling this budget-based approach with targeted model experiments could be an ideal strategy for determining the underlying controls for a host of annular mode behaviors.

Acknowledgments. We thank the editor and two anonymous reviewers whose comments have improved this manuscript. We acknowledge NASA for its provision of MERRA-2 data. Python libraries Numpy, matplotlib, and xarray expedited the analysis and visualization. This research was partially supported by Lilly Endowment, Inc., through its support for the Indiana University Pervasive Technology Institute. S. S. is supported under NASA FINESST Award 80NSSC21K1596, P. S. is supported under NSF Grant 1813981, and J. L. is supported by the DOE Office of Science Biological and Environmental Research as part of the Regional and Global Modeling and Analysis program area.

Data availability statement. MERRA-2 data are publicly available from NASA GES DISC (https://doi.org/10.5067/A7S6XP56VZWS; https://doi.org/10.5067/9NCR9DDDOPFI).

Code for computing the local wave activity budget is available from the corresponding author upon request.

REFERENCES

Andrews, D. G., C. B. Leovy, and J. R. Holton, 1987: *Middle Atmosphere Dynamics.* Academic Press, 489 pp.

Baldwin, M. P., and T. J. Dunkerton, 2001: Stratospheric harbingers of anomalous weather regimes. *Science*, **294**, 581–584, https://doi.org/10.1126/science.1063315.

——, D. B. Stephenson, and I. T. Jolliffe, 2009: Spatial weighting and iterative projection methods for EOFs. *J. Climate*, **22**, 234–243, https://doi.org/10.1175/2008JCLI2147.1.

Barnes, E. A., D. L. Hartmann, D. M. W. Frierson, and J. Kidston, 2010: Effect of latitude on the persistence of eddy-driven jets. *Geophys. Res. Lett.*, **37**, L11804, https://doi.org/10.1029/2010GL043199.

Blanco-Fuentes, J., and P. Zurita-Gotor, 2011: The driving of baroclinic anomalies at different timescales. *Geophys. Res. Lett.*, **38**, L23805, https://doi.org/10.1029/2011GL049785.

Bracegirdle, T. J., C. R. Holmes, J. S. Hosking, G. J. Marshall, M. Osman, M. Patterson, and T. Rackow, 2020: Improvements in circumpolar Southern Hemisphere extratropical atmospheric circulation in CMIP6 compared to CMIP5. *Earth Space Sci.*, **7**, e2019EA001065, https://doi.org/10.1029/2019EA001065.

Byrne, N. J., T. G. Shepherd, T. Woollings, and R. A. Plumb, 2016: Annular modes and apparent eddy feedbacks in the Southern Hemisphere. *Geophys. Res. Lett.*, **43**, 3897–3902, https://doi.org/10.1002/2016GL068851.

Chemke, R., and L. M. Polvani, 2019: Opposite tropical circulation trends in climate models and in reanalyses. *Nat. Geosci.*, **12**, 528–532, https://doi.org/10.1038/s41561-019-0383-x.

Feldstein, S. B., 1998: An observational study of the intraseasonal poleward propagation of zonal mean flow anomalies. *J. Atmos. Sci.*, **55**, 2516–2529, https://doi.org/10.1175/1520-0469(1998)055<2516:AOSOTI>2.0.CO;2.

Gelaro, R., and Coauthors, 2017: The Modern-Era Retrospective Analysis for Research and Applications, version 2 (MERRA-2). *J. Climate*, **30**, 5419–5454, https://doi.org/10.1175/JCLI-D-16-0758.1.

Gerber, E. P., L. M. Polvani, and D. Ancukiewicz, 2008: Annular mode time scales in the Intergovernmental Panel On Climate Change Fourth Assessment Report models. *Geophys. Res. Lett.*, **35**, L22707, https://doi.org/10.1029/2008GL035712.

Gritsun, A., and G. Branstator, 2007: Climate response using a three-dimensional operator based on the fluctuation–dissipation theorem. *J. Atmos. Sci.*, **64**, 2558–2575, https://doi.org/10.1175/JAS3943.1.

Hassanzadeh, P., and Z. Kuang, 2016: The linear response function of an idealized atmosphere. Part II: Implications for the practical use of the fluctuation–dissipation theorem and the role of operator's nonnormality. *J. Atmos. Sci.*, **73**, 3441–3452, https://doi.org/10.1175/JAS-D-16-0099.1.

Huang, C. S. Y., and N. Nakamura, 2016: Local finite-amplitude wave activity as a diagnostic of anomalous weather events. *J. Atmos. Sci.*, **73**, 211–229, https://doi.org/10.1175/JAS-D-15-0194.1.

——, and ——, 2017: Local wave activity budgets of the wintertime Northern Hemisphere: Implication for the Pacific and Atlantic storm tracks. *Geophys. Res. Lett.*, **44**, 5673–5682, https://doi.org/10.1002/2017gl073760.

Kidston, J., and E. P. Gerber, 2010: Intermodel variability of the poleward shift of the austral jet stream in the CMIP3 integrations linked to biases in 20th century climatology. *Geophys. Res. Lett.*, **37**, L09708, https://doi.org/10.1029/2010GL042873.

Kidson, J. W., 1988a: Indices of the Southern Hemisphere zonal wind. *J. Climate*, **1**, 183–194, https://doi.org/10.1175/1520-0442(1988)001<0183:IOTSHZ>2.0.CO;2.

——, 1988b: Interannual variations in the Southern Hemisphere circulation. *J. Climate*, **1**, 1177–1198, https://doi.org/10.1175/1520-0442(1988)001<1177:IVITSH>2.0.CO;2.

Lee, S., and S. Feldstein, 1996: Mechanism of zonal index evolution in a two-layer model. *J. Atmos. Sci.*, **53**, 2232–2246, https://doi.org/10.1175/1520-0469(1996)053<2232:MOZIEI>2.0.CO;2.

——, S.-W. Son, K. Grise, and S. B. Feldstein, 2007: A mechanism for the poleward propagation of zonal mean flow anomalies. *J. Atmos. Sci.*, **64**, 849–868, https://doi.org/10.1175/JAS3861.1.

Li, Y., and D. W. J. Thompson, 2016: Observed signatures of the barotropic and baroclinic annular modes in cloud vertical structure and cloud radiative effects. *J. Climate*, **29**, 4723–4740, https://doi.org/10.1175/JCLI-D-15-0692.1.

——, ——, Y. Huang, and M. Zhang, 2014: Observed linkages between the northern annular mode/North Atlantic oscillation, cloud incidence, and cloud radiative forcing. *Geophys. Res. Lett.*, **41**, 1681–1688, https://doi.org/10.1002/2013GL059113.

Liu, S., P. W. Staten, and B. H. Kahn, 2020: Improved detection of interannual cloud variability over the Southern Hemisphere using legacy satellites. *J. Climate*, **33**, 8225–8236, https://doi.org/10.1175/JCLI-D-19-0758.1.

Lorenz, D. J., 2023a: A simple mechanistic model of wave–mean flow feedbacks, poleward jet shifts, and the annular mode. *J. Atmos. Sci.*, **80**, 549–568, https://doi.org/10.1175/JAS-D-22-0056.1.

——, 2023b: Dynamics of the transient negative eddy response to zonal-mean zonal wind variations. *J. Atmos. Sci.*, **80**, 593–610, https://doi.org/10.1175/JAS-D-22-0084.1.

——, and D. L. Hartmann, 2001: Eddy–zonal flow feedback in the Southern Hemisphere. *J. Atmos. Sci.*, **58**, 3312–3327, https://doi.org/10.1175/1520-0469(2001)058<3312:EZFFIT>2.0.CO;2.

Lu, J., G. Chen, L. R. Leung, D. Burrows, Q. Yang, K. Sakaguchi, and S. Hagos, 2015: Toward the dynamical convergence on the jet stream in aquaplanet AGCMs. *J. Climate*, **28**, 6763–6782, 150701152506008, https://doi.org/10.1175/JCLI-D-14-00761.1.

Lubis, S. W., and P. Hassanzadeh, 2021: An eddy–zonal flow feedback model for propagating annular modes. *J. Atmos. Sci.*, **78**, 249–267, https://doi.org/10.1175/JAS-D-20-0214.1.

Lutsko, N. J., and M. C. Hell, 2021: Moisture and the persistence of annular modes. *J. Atmos. Sci.*, **78**, 3951–3964, https://doi.org/10.1175/JAS-D-21-0055.1.

Ma, D., P. Hassanzadeh, and Z. Kuang, 2017: Quantifying the eddy–jet feedback strength of the annular mode in an idealized GCM and reanalysis data. *J. Atmos. Sci.*, **74**, 393–407, https://doi.org/10.1175/JAS-D-16-0157.1.

Nakamura, N., and A. Solomon, 2010: Finite-amplitude wave activity and mean flow adjustments in the atmospheric general circulation. Part I: Quasigeostrophic theory and analysis. *J. Atmos. Sci.*, **67**, 3967–3983, https://doi.org/10.1175/2010JAS3503.1.

——, and D. Zhu, 2010: Finite-amplitude wave activity and diffusive flux of potential vorticity in eddy–mean flow interaction. *J. Atmos. Sci.*, **67**, 2701–2716, https://doi.org/10.1175/2010JAS3432.1.

——, and C. S. Y. Huang, 2017: Local wave activity and the onset of blocking along a potential vorticity front. *J. Atmos. Sci.*, **74**, 2341–2362, https://doi.org/10.1175/JAS-D-17-0029.1.

——, and ——, 2018: Atmospheric blocking as a traffic jam in the jet stream. *Science*, **361**, 42–47, https://doi.org/10.1126/science.aat0721.

Nie, Y., Y. Zhang, G. Chen, X.-Q. Yang, and D. A. Burrows, 2014: Quantifying barotropic and baroclinic eddy feedbacks in the persistence of the Southern Annular Mode. *Geophys. Res. Lett.*, **41**, 8636–8644, https://doi.org/10.1002/2014GL062210.

Palipane, E., J. Lu, P. Staten, G. Chen, and E. K. Schneider, 2017: Investigating the zonal wind response to SST warming using transient ensemble AGCM experiments. *Climate Dyn.*, **48**, 523–540, https://doi.org/10.1007/s00382-016-3092-9.

Papavasileiou, G., A. Voigt, and P. Knippertz, 2020: The role of observed cloud-radiative anomalies for the dynamics of the North Atlantic oscillation on synoptic time-scales. *Quart. J. Roy. Meteor. Soc.*, **146**, 1822–1841, https://doi.org/10.1002/qj.3768.

Riehl, H., T. C. Yeh, and N. E. La seur, 1950: A study of variations of the general circulation. *J. Atmos. Sci.*, **7**, 181–194, https://doi.org/10.1175/1520-0469(1950)007<0181:ASOVOT>2.0.CO;2.

Ring, M. J., and R. A. Plumb, 2008: The response of a simplified GCM to axisymmetric forcings: Applicability of the fluctuation–dissipation theorem. *J. Atmos. Sci.*, **65**, 3880–3898, https://doi.org/10.1175/2008JAS2773.1.

Robert, L., G. Rivière, and F. Codron, 2017: Positive and negative eddy feedbacks acting on midlatitude jet variability in a three-level quasigeostrophic model. *J. Atmos. Sci.*, **74**, 1635–1649, https://doi.org/10.1175/JAS-D-16-0217.1.

Robinson, W. A., 2000: A baroclinic mechanism for the eddy feedback on the zonal index. *J. Atmos. Sci.*, **57**, 415–422, https://doi.org/10.1175/1520-0469(2000)057<0415:ABMFTE>2.0.CO;2.

Rossby, C. G., and H. C. Willett, 1948: The circulation of the upper troposphere and lower stratosphere. *Science*, **108**, 643–652, https://doi.org/10.1126/science.108.2815.643.

Saggioro, E., and T. G. Shepherd, 2019: Quantifying the timescale and strength of Southern Hemisphere intraseasonal stratosphere-troposphere coupling. *Geophys. Res. Lett.*, **46**, 13 479–13 487, https://doi.org/10.1029/2019GL084763.

Sheshadri, A., and R. A. Plumb, 2017: Propagating annular modes: Empirical orthogonal functions, principal oscillation patterns, and time scales. *J. Atmos. Sci.*, **74**, 1345–1361, https://doi.org/10.1175/JAS-D-16-0291.1.

Simpson, I. R., and L. M. Polvani, 2016: Revisiting the relationship between jet position, forced response, and annular mode variability in the southern midlatitudes. *Geophys. Res. Lett.*, **43**, 2896–2903, https://doi.org/10.1002/2016GL067989.

——, T. G. Shepherd, P. Hitchcock, and J. F. Scinocca, 2013: Southern annular mode dynamics in observations and models. Part II: Eddy feedbacks. *J. Climate*, **26**, 5220–5241, https://doi.org/10.1175/JCLI-D-12-00495.1.

Smith, S., P. W. Staten, and J. Lu, 2021: How moist and dry intrusions control the local hydrologic cycle in present and future climates. *J. Climate*, **34**, 4343–4359, https://doi.org/10.1175/JCLI-D-20-0780.1.

Son, S.-W., and S. Lee, 2006: Preferred modes of variability and their relationship with climate change. *J. Climate*, **19**, 2063–2075, https://doi.org/10.1175/JCLI3705.1.

Sparrow, S., M. Blackburn, and J. D. Haigh, 2009: Annular variability and eddy–zonal flow interactions in a simplified atmospheric GCM. Part I: Characterization of high- and low-frequency behavior. *J. Atmos. Sci.*, **66**, 3075–3094, https://doi.org/10.1175/2009JAS2953.1.

Thompson, D. W. J., and J. M. Wallace, 2000: Annular modes in the extratropical circulation. Part I: Month-to-month variability. *J. Climate*, **13**, 1000–1016, https://doi.org/10.1175/1520-0442(2000)013<1000:AMITEC>2.0.CO;2.

——, ——, and G. C. Hegerl, 2000: Annular modes in the extratropical circulation. Part II: Trends. *J. Climate*, **13**, 1018–1036, https://doi.org/10.1175/1520-0442(2000)013<1018:AMITEC>2.0.CO;2.

Wang, L., and N. Nakamura, 2015: Covariation of finite-amplitude wave activity and the zonal mean flow in the midlatitude troposphere: 1. Theory and application to the Southern Hemisphere summer. *Geophys. Res. Lett.*, **42**, 8192–8200, https://doi.org/10.1002/2015GL065830.

Woollings, T., L. Papritz, C. Mbengue, and T. Spengler, 2016: Diabatic heating and jet stream shifts: A case study of the 2010 negative North Atlantic oscillation winter. *Geophys. Res. Lett.*, **43**, 9994–10 002, https://doi.org/10.1002/2016GL070146.

Xia, X., and E. K. M. Chang, 2014: Diabatic damping of zonal index variations. *J. Atmos. Sci.*, **71**, 3090–3105, https://doi.org/10.1175/JAS-D-13-0292.1.

Zurita-Gotor, P., J. Blanco-Fuentes, and E. P. Gerber, 2014: The impact of baroclinic eddy feedback on the persistence of jet variability in the two-layer model. *J. Atmos. Sci.*, **71**, 410–429, https://doi.org/10.1175/JAS-D-13-0102.1.